University of Denver
Digital Commons @ DU

Electronic Theses and Dissertations | Graduate Studies

1-1-2010

Influence of Compressible Aerogel Electrodes on the Properties of an Electrochemical Cell

Chris Sponheimer
University of Denver

Follow this and additional works at: https://digitalcommons.du.edu/etd

 Part of the Biomaterials Commons

Recommended Citation

Sponheimer, Chris, "Influence of Compressible Aerogel Electrodes on the Properties of an Electrochemical Cell" (2010). *Electronic Theses and Dissertations*. 620.
https://digitalcommons.du.edu/etd/620

This Dissertation is brought to you for free and open access by the Graduate Studies at Digital Commons @ DU. It has been accepted for inclusion in Electronic Theses and Dissertations by an authorized administrator of Digital Commons @ DU. For more information, please contact jennifer.cox@du.edu,dig-commons@du.edu.

Influence of Compressible Aerogel Electrodes on the Properties of an Electrochemical Cell

_____

A Dissertation

Presented to

the faculty of Engineering and Computer Science

University of Denver

_____

In Partial Fulfillment

of the Requirements for the Degree

Doctor of Philosophy

_____

by

Christopher Sponheimer

June 2010

Advisor: Corinne Lengsfeld

©Copyright by Christopher Sponheimer 2010

All Rights Reserved

Author: Christopher Sponheimer
Title: Influence of Compressible Aerogel Electrodes on the Properties of an Electrochemical Cell
Advisor: Corinne Lengsfeld
Degree Date: June 2010

ABSTRACT

In the biomedical field the need for intra organ pressure measurement can only be facilitated by adapting existing pressure sensing technology to the specific tissues under test. The customization of these sensors has only driven up cost and the need to explore new technologies has become increasingly more important. For this dissertation, we explore the use of a new technology, particularly electrochemical pressure sensing to provide a low-cost pressure sensor to fill this need. Preliminary testing showed that electrically conductive polymers exhibited a change in voltage when pressurized if bubbles were first electrolyzed in the gel creating an aerogel, and that this effect was virtually undetectable without the bubbles present. Using electrochemical impedance spectroscopy (EIS) and model fitting, it was shown that this effect occurs at the electrode interface. Theoretical derivation supported by potentiostatic voltage measurements indicated that a change in the electrode surface area in contact with the fluid was responsible for the effect. Optical micrographs were taken as a bubble along the electrode was pressurized. Using image analysis, the relationship of the change in surface area of the bubble correlated to the relationship of the change in impedance of the electrochemical cell (ECC). The results further demonstrated that the electrochemical response to pressure of a gelatin aerogel electrode was linear for the pressure range of 0 to1034 mmHg. This finding lends itself well for use in medical devices. A new device was invented along with a manufacturing process for an electrochemical pressure

transducer (EPT). The EPT was subject to *in vitro* testing using simulated gastric fluid to create a baseline efficacy of the device for use in the gastrointestinal tract. Multiple design specific techniques were developed to improve sensor performance during physiological conditions.

Acknowledgements

This dissertation is a tremendous accomplishment in my life and should be recognized that it could not have been possible without the generous help of the following people:

Corinne Lengsfeld	For the faith and confidence that you placed in me to undertake such a challenging project and the intellectual support to help see it through to completion.
Jamee Sponheimer	For making such a huge sacrifice to allow me to pursuit my dreams.
Mom and Dad	For the moral support and helping me become the person I am today.
Michelle Zeles-Hahn	For your guidance and leadership.
Matt Opgenorth	For helping with whatever problems I was presented with.
Jon Buckley	For the time and effort ensuring I had the best fixtures and equipment to run my experiments.
Brian Burks	For taking time out of your own projects to help me complete my own.
Committee Members	For your advisement to overcome my technical obstacles.

Table of Contents

LIST OF FIGURES VII
LIST OF TABLES XI

1 INTRODUCTION 1

1.1 Existing Technology 1
1.2 Electrochemomechanical Pressure Transducers 3
1.3 Gelatin Based Electrochemical Cell 4
1.4 Summary of Research Goals 5

2 ELECTROCHEMICAL ANALYSIS OF THE GELATIN HYDROGEL-AEROGEL INTERFACE 7

2.1 Introduction 7
2.2 Materials 8
2.3 Methods 9
Preparation of Gelatin Hydrogels 9
Light Transmission through Gel Cured at Atmospheric Pressure and Vacuum 10
Determination of Effective Gelatin Diameter 10
Viscosity Measurement 10
Electrolysis 11
Electrochemical Impedance Spectroscopy 13
Modeling the Equivalent Circuit 16
Methods for Establishing the Initial Guess 18
Open Circuit Voltage 19
2.4 Results 20
2.5 Discussion 27
2.6 Conclusion 33

3 MECHANICAL ANALYSIS OF THE GELATIN HYDROGEL-AEROGEL INTERFACE 35

3.1 Introduction 35
3.2 Materials 39
3.3 Methods 39
Experimental Setup 39
Preparation of Gelatin Hydrogels 40
Bubble Stability 41
Imagery 41
Image Analysis 42
3.4 Results 44
3.5 Discussion 50
3.6 Conclusions 53

4 EFFICACY OF AN ELECTROCHEMOMECHANICAL PRESSURE TRANSDUCER FOR USE IN THE GASTROINTESTINAL TRACT 54

4.1 Introduction 54
4.2 Materials 59
4.3 Methods 59
Preparation of Gelatin Hydrogels 59
Current Measurement 60
Impedance Measurement 60
Gastric Simulation 61
4.4 Results 62
4.5 Discussion 71
4.6 Conclusions 76

5 CONCLUSION 77

REFERENCES 79

List of Figures

FIGURE 2.1 – POURBAIX DIAGRAM OF ALUMINUM AT 25 ^{O}C IN WATER REPRODUCED FROM [17]. THE REVERSIBLE REACTIONS ARE INDICATED BY A LETTER OR NUMBER ENCLOSED BY A CIRCLE. THE LINE ASSOCIATED WITH EACH OF THE REACTIONS DESIGNATES THE BOUNDARY FOR THE CONDITIONS IN TERMS OF VOLTAGE AND PH AT WHICH THE REACTION WILL OCCUR. 12

FIGURE 2.2 – RANDLES CIRCUIT DIAGRAM: C_{BULK} REPRESENTS THE BULK CAPACITANCE, C_{DL} REPRESENTS THE DOUBLE LAYER CAPACITANCE, R_{BULK} REPRESENTS THE BULK RESISTANCE, R_{CT} REPRESENTS THE CHARGE TRANSFER RESISTANCE AND W_{INF} REPRESENTS THE NON-LINEAR WARBURG IMPEDANCE. THE HYPHENATED SUBSCRIPT R REPRESENTS THE REFERENCE ELECTRODE WHEREAS THE W REPRESENTS THE WORKING ELECTRODE. 14

FIGURE 2.3 – DIAGRAM OF EIS TEST SETUP. A GLASS CELL IS SHOWN IN THE CENTER OF A HEATED WATER BATH. TWO INSULATED ELECTRODES MAKE CONTACT WITH THE GELATIN HYDROGEL INSIDE THE GLASS CELL. A PORT IN THE GLASS CELL ALLOWS A NITROGEN GAS SUPPLY TO PRESSURIZE THE GEL. 16

FIGURE 2.4 – GRAPHICAL REPRESENTATION OF THE FRINGE EFFECT. THE SOLID RECTANGLES REPRESENT ELECTRIC CONDUCTORS AND THE LINES BETWEEN THE CONDUCTORS REPRESENT THE ELECTRIC FIELD FLUX. 19

FIGURE 2.5 – PLOT OF OCV VERSUS TIME OF AN ECC WITH 17.5% GELATIN AND TWO ALUMINUM ELECTRODES AT 25 ^{O}C. THE X-AXIS ALONG THE BOTTOM OF THE PLOT IS LINEAR WITH A RANGE OF 0 TO 20 HOURS. THE Y-AXIS ALONG THE LEFT-HAND SIDE OF THE PLOT IS ALSO LINEAR WITH A RANGE OF -0.01 TO 0.07 VOLTS. THE RAW DATA FOR VOLTAGE IS REPRESENTED BY A BLUE LINE. 20

FIGURE 2.6 – PLOT OF IMPEDANCE AND PHASE ANGLE VERSUS FREQUENCY OF AN ECC WITH 17.5% GELATIN, TWO ALUMINUM ELECTRODES, PRESSURIZED TO 517 MMHG AT 25 ^{O}C. THE X-AXIS ALONG THE BOTTOM OF THE PLOT IS LOGARITHMIC WITH A RANGE OF 100 MHZ TO 100 KHZ. THE Y-AXIS ALONG THE LEFT-HAND SIDE OF THE PLOT IS LOGARITHMIC WITH A RANGE OF 1.00 K OHM TO 10 M OHM. THE Y-AXIS ON THE RIGHT-HAND SIDE OF THE PLOT IS LINEAR WITH A RANGE OF -80^{O} TO 20^{O}. THE RAW DATA FOR IMPEDANCE IS REPRESENTED BY OPEN BLUE CIRCLES, WHILE THE RAW DATA FOR PHASE ANGLE IS REPRESENTED BY OPEN RED SQUARES. THE RANDLE'S CIRCUIT MODEL FIT IS REPRESENTED BY A RED DASHED-LINE AND A BLUE DASHED-LINE FOR THE IMPEDANCE AND PHASE ANGLE RESPECTIVELY. THE RANDLE'S CIRCUIT WITH WARBURG TERMS MODEL FIT IS REPRESENTED BY A RED LINE AND A BLUE LINE FOR THE IMPEDANCE AND PHASE ANGLE RESPECTIVELY. 21

FIGURE 2.7 – PLOT OF IMPEDANCE AND PHASE ANGLE VERSUS FREQUENCY OF AN ECC WITH 17.5% GELATIN, TWO ALUMINUM ELECTRODES, AT 25 ^{O}C. THE X-AXIS ALONG THE BOTTOM OF THE PLOT IS LOGARITHMIC WITH A RANGE OF 100 MHZ TO 100 KHZ. THE Y-AXIS ALONG THE LEFT-HAND SIDE OF THE PLOT IS LOGARITHMIC WITH A RANGE OF 1 K OHM TO 10 M OHM. THE Y-AXIS ON THE RIGHT-HAND SIDE OF THE PLOT IS LINEAR WITH A RANGE OF -100^{O} TO 20^{O}. THE RAW DATA FOR IMPEDANCE IS REPRESENTED BY OPEN BLUE CIRCLES AND SOLID BLUE CIRCLES, AT PRESSURES OF 0 MMHG AND 517 MMHG RESPECTIVELY. THE RAW DATA FOR PHASE ANGLE IS REPRESENTED BY OPEN RED SQUARES AND SOLID RED DIAMONDS, AT PRESSURE OF 0 MMHG AND 517 MMHG RESPECTIVELY. 23

FIGURE 2.8 – PLOT OF IMPEDANCE AND PHASE ANGLE VERSUS FREQUENCY OF AN ECC WITH 17.5% GELATIN, TWO ALUMINUM ELECTRODES, AT 25 ^{O}C. THE X-AXIS ALONG THE BOTTOM OF THE PLOT IS LOGARITHMIC WITH A RANGE OF 100.0 MHZ TO 100 KHZ. THE Y-AXIS ALONG THE LEFT-HAND SIDE OF THE PLOT IS LOGARITHMIC WITH A RANGE OF 1 K OHM TO 10 M OHM. THE Y-AXIS ON THE TIGHT-HAND SIDE OF THE PLOT IS LINEAR WITH A RANGE OF -80^{O} TO 20^{O}. THE RAW DATA FOR IMPEDANCE IS REPRESENTED BY OPEN DARK BLUE CIRCLES, SOLID BLUE CIRCLES AND OPEN LIGHT BLUE CIRCLES, AT PRESSURE OF 0 MMHG, 517 MMHG, AND THEN 0 MMHG RESPECTIVELY. THE RAW DATA FOR PHASE

ANGLE IS REPRESENTED BY OPEN RED SQUARES, SOLID RED DIAMONDS, AND OPEN ORANGE SQUARES, AT PRESSURE OF 0 MMHG, 517 MMHG, AND 0 MMHG RESPECTIVELY. 24

FIGURE 2.9 – PLOT OF OCV VERSUS TIME OF AN ECC WITH 17.5% GELATIN, TWO ALUMINUM ELECTRODES, AT 25 ^{O}C. THE X-AXIS AT THE BOTTOM OF THE PLOT HAS A RANGE OF 0 SECONDS TO 1000 SECONDS. THE Y-AXIS ON THE RIGHT-HAND SIDE OF THE PLOT HAS A RANGE OF -217 MV TO -213 MV, THE VALUE OF THE PRESSURE IMPULSE IS NOT SHOWN IN THIS PLOT. 26

FIGURE 2.10 – PLOT OF THE CHANGE IN OCV VERSUS THE CHANGE IN APPLIED PRESSURE IN AN ECC WITH 17.5% GELATIN, TWO ALUMINUM ELECTRODES, AT 25 ^{O}C. THE X-AXIS AT THE BOTTOM OF THE PLOT HAS A RANGE OF 0 TO 600 MMHG. THE Y-AXIS ON THE LEFT-HAND SIDE OF THE PLOT HAS A RANGE OF 0 MV TO 4 MV. EACH SOLID BLUE CIRCLE REPRESENTS THE RAW DATA. A LEAST SQUARED LINEAR REGRESSION LINE IS PLOTTED THROUGH THE DATA AND IS THE REPORTED ON THE PLOT ALONG WITH THE COEFFICIENT OF DETERMINATION DENOTED R^2. 26

FIGURE 2.11 – PLOT OF IMPEDANCE AND PHASE ANGLE FROM FIGURE 2.7 WITH A FREQUENCY RANGE OF 10 TO 100 HZ....29

FIGURE 2.12 – PLOT OF IMPEDANCE AND PHASE ANGLE FROM FIGURE 2.8 WITH A FREQUENCY RANGE OF 10 TO 100 HZ....30

FIGURE 2.13 – PLOT OF OCV VERSUS TIME OF AN ECC WITH 17.5% GELATIN, TWO ALUMINUM ELECTRODES, AT 25 ^{O}C. THE X-AXIS AT THE BOTTOM OF THE PLOT HAS A RANGE OF 1800 SECONDS TO 2300 SECONDS. THE Y-AXIS ON THE RIGHT-HAND SIDE OF THE PLOT HAS A RANGE OF -220 MV TO -216.0 MV THE VALUE OF THE PRESSURE IMPULSE IS NOT SHOWN IN THIS PLOT. 33

FIGURE 3.1 – ILLUSTRATIVE REPRESENTATION OF A BUBBLE ON THE ELECTRODE SURFACE IN A GELATIN HYDROGEL. THE FIRST SCENARIO DEPICTED IN 3.1 A, SHOWS THE BUBBLE DISPLACING THE VOLUME OF LIQUID BETWEEN THE GELATIN NETWORK, WHEREAS 3.1 B, SHOWS THE BUBBLE DISPLACING THE VOLUME IN AND AROUND THE GELATIN NETWORK FORMING AN AEROGEL. 36

FIGURE 3.2 – FRONT VIEW MICROGRAPHS OF A BUBBLE ON TOP OF AN ANODE IN AN ECC, ALL IMAGES WERE TAKEN AT 25 ^{O}C AND 0 MMHG. IMAGE A IS THE ORIGINAL MICROGRAPH, IMAGE B IS AN ENHANCED IMAGE OF THE ORIGINAL MICROGRAPH, IMAGE C IS THE BLACK AND WHITE CONVERSION OF THE ENHANCED IMAGE, AND IMAGE D IS THE ORIGINAL MICROGRAPH WITH THE EDGE BOUNDARY SUPERIMPOSED ON IT. 44

FIGURE 3.3 – TOP VIEW PHOTOGRAPHS OF OXYGEN BUBBLES ON THE ANODE SURFACE TAKEN OVER A PERIOD OF 4 DAYS. 45

FIGURE 3.4 – TOP VIEW PHOTOGRAPHS OF HYDROGEN BUBBLES ON THE CATHODE SURFACE TAKEN OVER A PERIOD OF 4 HOURS. 46

FIGURE 3.5 – TOP VIEW PHOTOGRAPHS OF AIR BUBBLES IN THE BULK SOLUTION TAKEN OVER A PERIOD OF 5 DAYS....46

FIGURE 3.6 – FRONT VIEW ENHANCED BLACK AND WHITE MICROGRAPHS OF A BUBBLE ON TOP OF AN ANODE IN AN ECC, ALL IMAGES WERE TAKEN AT 25 ^{O}C. IMAGES A – N WERE TAKEN AT INCREASING PRESSURIZATION FROM 0 TO 280 MMHG AT 20 MMHG INCREMENTS. NOTE: AN IMAGE WAS NOT TAKEN AT 160 MMHG....47

FIGURE 3.7 – PLOT OF THE CHANGE IN VOLUME VERSUS THE CHANGE IN APPLIED PRESSURE IN AN ECC WITH 17.5% GELATIN, TWO ALUMINUM ELECTRODES, AT 25 ^{O}C. THE X-AXIS AT THE BOTTOM OF THE PLOT HAS A RANGE OF 0 MMHG TO 300 MMHG. THE Y-AXIS ON THE RIGHT-HAND SIDE OF THE PLOT HAS A RANGE OF 3 μL TO 5 μL. EACH SOLID BLUE CIRCLE REPRESENTS THE RAW DATA. 48

FIGURE 3.8 – PLOT OF THE CHANGE IN SURFACE AREA VERSUS THE CHANGE IN APPLIED PRESSURE IN AN ECC WITH 17.5% GELATIN, TWO ALUMINUM ELECTRODES, AT 25 ^{O}C. THE X-AXIS AT THE BOTTOM OF THE PLOT HAS A RANGE OF 0 TO 300 MMHG. THE Y-AXIS ON THE LEFT-HAND SIDE OF THE PLOT HAS A RANGE OF 7.8 MM^2 TO 9.4 MM^2. EACH SOLID BLUE CIRCLE REPRESENTS THE RAW DATA. A LEAST SQUARED LINEAR REGRESSION LINE IS PLOTTED THROUGH THE DATA AND IS THE REPORTED ON THE PLOT ALONG WITH THE COEFFICIENT OF DETERMINATION DENOTED R^2. 49

FIGURE 3.9 – PLOT OF THE CHANGE IN IMPEDANCE VERSUS THE CHANGE IN APPLIED PRESSURE IN AN ECC WITH 17.5% GELATIN, TWO ALUMINUM ELECTRODES, AT 25 ^{O}C. THE X-AXIS AT THE BOTTOM OF THE PLOT HAS A RANGE OF 0 TO 300 MMHG. THE Y-AXIS ON THE LEFT-HAND SIDE OF THE PLOT HAS A RANGE OF 0 TO 800 OHMS. EACH SOLID BLUE CIRCLE REPRESENTS THE RAW DATA. A LEAST SQUARED LINEAR REGRESSION LINE IS PLOTTED THROUGH THE DATA AND IS THE REPORTED ON THE PLOT ALONG WITH THE COEFFICIENT OF DETERMINATION DENOTED R^2. 50

FIGURE 4.1 – ANATOMICAL DIAGRAM OF THE SWALLOWING PROCESS [52]. 55

FIGURE 4.2 – ILLUSTRATION OF EPT 62

FIGURE 4.3 – PLOT OF CURRENT VERSUS TIME WITH AN APPLIED POTENTIAL OF 250 MV. THE ECC WAS PRESSURIZED 4 TIMES AT 517 MMHG AT 10 AND 20 SECOND INTERVALS 63

FIGURE 4.4 – PLOTS OF IMPEDANCE VERSUS TIME. PLOT A REFERS TO A 100 HZ TEST SIGNAL, WHILE PLOT B REFERS TO A 500 HZ TEST SIGNAL. IN EACH PLOT THE BLUE AND RED LINES ARE THE MEASURED TOTAL AND REAL COMPONENTS OF THE IMPEDANCE RESPECTIVELY. THE LEFT AXIS IS IN OHMS AND CORRESPONDS TO THE TOTAL IMPEDANCE; THE RIGHT IS ALSO IN OHMS AND CORRESPONDS TO THE REAL COMPONENT OF IMPEDANCE. IN EACH PLOT THE ECC WAS PRESSURIZED TO 517 MMHG DURING THE TIME FRAME BETWEEN 30 AND 60 SECONDS. 65

FIGURE 4.5 – BAR GRAPH OF THE PERCENT CHANGE IN IMPEDANCE DUE TO A 517 MMHG PRESSURE IMPULSE. THE BLUE BARS REPRESENT THE REAL COMPONENT OF THE IMPEDANCE, WHILE THE RED BARS REPRESENT THE TOTAL IMPEDANCE. EACH SET OF BARS ARE GRAPHED NEXT TO THEIR ASSOCIATED FREQUENCY. 66

FIGURE 4.6 – BAR GRAPH OF THE PERCENT CHANGE IN DRIFT DUE TO A 517 MMHG PRESSURE IMPULSE. THE BLUE BARS REPRESENT THE REAL COMPONENT OF THE IMPEDANCE, WHILE THE RED BARS REPRESENT THE TOTAL IMPEDANCE. EACH SET OF BARS ARE GRAPHED NEXT TO THEIR ASSOCIATED FREQUENCY. 66

FIGURE 4.7 – BAR GRAPH OF THE SIGNAL TO NOISE RATIO OF THE DRIFT FOR EACH FREQUENCY. THE BLUE BARS REPRESENT THE REAL COMPONENT OF THE IMPEDANCE, WHILE THE RED BARS REPRESENT THE TOTAL IMPEDANCE. THE SNR IS REPORTED IN DECIBELS. 67

FIGURE 4.8 – PLOT OF TOTAL IMPEDANCE VERSUS TIME, THE GASTRIC IMPEDANCE WAS MEASURED FROM AN EPT SUBMERSED IN SIMULATED GASTRIC FLUID, WHILE THE AIR IMPEDANCE WAS MEASURED FROM AN EPT SUSPENDED ABOVE AND NOT TOUCHING THE SIMULATED GASTRIC FLUID. TIME IS PLOTTED ON A LOG (BASE 2) SCALE. 69

FIGURE 4.9 – PLOT OF CHANGE IN IMPEDANCE VERSUS TIME, THE GASTRIC IMPEDANCE WAS MEASURED FROM AN EPT SUBMERSED IN SIMULATED GASTRIC FLUID, WHILE THE AIR IMPEDANCE WAS MEASURED FROM AN EPT SUSPENDED ABOVE AND NOT TOUCHING THE SIMULATED GASTRIC FLUID. TIME IS PLOTTED ON A LOG (BASE 2) SCALE. 69

FIGURE 4.10 – PLOT OF IMPEDANCE VERSUS TIME, THE IMPEDANCE WAS MEASURED FROM AN EPT THAT WAS SUBMERSED IN SIMULATED GASTRIC FLUID WHILE THE GLASS CELL WAS PRESSURIZED THREE TIMES TO 517 MMHG. 70

FIGURE 4.11 – PLOT OF IMPEDANCE VERSUS TIME, THE GASTRIC IMPEDANCE WAS MEASURED FROM AN EPT THAT WAS SUSPENDED ABOVE SIMULATED GASTRIC FLUID WHILE THE GLASS CELL WAS PRESSURIZED THREE TIMES TO 517 MMHG. 70

List of Tables

TABLE 2.1 – CIRCUIT COMPONENT VALUES WITH THEIR ASSOCIATE ERROR FROM RANDLES CIRCUIT AND RANDLE'S CIRCUIT WITH WARBURG TERMS MODEL FIT. 22

TABLE 2.2 – CIRCUIT COMPONENT VALUES WITH THEIR ASSOCIATE ERROR FROM THE RANDLE'S CIRCUIT MODEL FIT FOR EACH SET OF DATA PLOTTED IN FIGURE 2.8.....25

TABLE 4.1 – PRESSURE AND IMPEDANCE OF ECC FOR PRESSURE RANGE TEST. THE IMPEDANCE WAS MEASURED 10 SECONDS AFTER THE PRESSURE WAS OBTAINED. THE GLASS CELL SHATTERED BETWEEN PRESSURES OF 2586 AND 3100 AND THE IMPEDANCE WAS MEASURED AFTER THE PRESSURE RETURNED TO ATMOSPHERIC. 68

1 Introduction

Medical diagnostic equipment has evolved to the point where noninvasive techniques can image tissue and determine both composition and the spatial organization of the material. However, science has not evolved to the point where direct internal force or pressure measurements can be taken in living subjects. To provide this information, sensors must be placed directly in the path of the exerted force inside the desired tissue. To achieve this end, special considerations must be taken into account to minimize extraneous effects that the sensor may have on the tissue. Safety issues must be addressed, for example the sensor should be biocompatible and the risk of electrical shock should be minimized. Additionally, the footprint of the sensor should be adequately sized for the tissue to be measured. It must be small enough not to create additional stress on neighboring tissue, have a similar modulus to reduce stress shielding and thereby reducing stress concentrations, and be flexible enough to uncouple pressure from applied bending moments.

1.1 Existing Technology

The current trend in medical pressure sensors and pressure sensors in general is miniaturization. By taking the principals used in their macro counterparts, pressure sensors have been miniaturized down to the microscale, and in some cases down to the nanoscale. While miniaturization has allowed these sensors to overcome some of the

drawbacks with invasive pressure sensing, some of the properties are inherent regardless of the size.

Pressure is simply the flux of force over a given area, and the premise behind pressure measurement is that this force will cause a displacement on the sensor. The discovery of the piezoresistive effect in 1954 led to the commercialization of the piezoresistive sensor [1]. A piezoresistor composed of silicon and germanium is mounted on a deformable diaphragm. As the diaphragm deforms due to a pressure differential, the total length of the piezoresistor lengthens or shortens in the direction of the electrical potential causing a subsequent change in the electrical resistance. In order to take advantage of the change in resistance, a voltage must be constantly applied across the piezoresistor. Although in the early 1970s silicon etching technologies allowed for microscopic designs, the sensors were limited to rigid 2-dimensional substrates [2-4]. These sensors can sense pressure well when the applied force is normal to the surface or in a fluid with constant pressure. However, when the sensors are located in a collapsible organ, forces are not equal and the sensor will not capture all pressures surrounding the sensor.

Capacitive based pressure sensors operate on the principal of having two parallel conductive plates separated by an elastic dielectric material. As a pressure is applied, the plates move closer to each other and increase the capacitance [5]. Similarly to resistive pressure sensors an electric field must be applied to measure the capacitance; thus suffers from the same issues as the piezoresistive sensors.

Optical pressure sensors operate on the principal of interferometry [6, 7]. It comprises a light source a reflector on a deformable diaphragm and a detector. As the

diaphragm deforms, the light that is reflected back becomes out of phase. By measuring this angle, the pressure can be calculated. One of the largest obstacles for this technology is providing the light source to the sensor and a spectrum analyzer to measure the response; as a result this technique is not cost effective.

1.2 Electrochemomechanical Pressure Transducers

Electrically conductive polymers have several attributes over the materials used in traditional pressure sensors which make them attractive for use in biological systems. Electrochemical pressure transducers (EPT) are passive and have the ability to generate a voltage potential in response to pressure. From an electrical safety point of view, this means that the sensors do not require low impedance power supply lines routed inside the body to the sensor. With exception to the electrodes, EPTs are comprised of soft deformable materials. This allows the sensor to interface to soft tissue better than the rigid silicon based sensors. Also by lacking a rigid substrate, the EPTs do not necessarily have a preferential sensing direction and can be designed for omni-directional measurements.

The measurable elctrochemomechanical (ECM) response is a reversible process in which changes in electrical current result from a change in chemical composition as a response to mechanical stimulation. In the early 1990's researchers began investigating the use of electrically conductive polymers for pressure sensing applications [8, 9]. When an electrically conductive polymer such as polypyrrole undergoes mechanical deformation, the volume will change accordingly. An expansion in the film results in a dilution in the surface concentration of mobile ions, while a contraction results in an

increase in the surface concentration of mobile ions [10]. By correlating the change in current through the system to mechanical force, the film can act as a pressure sensor.

1.3 Gelatin Based Electrochemical Cell

Modern ECM literature on voltage response density from using polypyrrole and similar synthetic electrically conductive polymers report values in the neighborhood of 6 V/m^2 while straining the polymer 20% [9]. For these measurements voltage density was taken as the peak voltage change divided by the total surface area of both electrodes. Using a Young's Modulus of 180 MPa for wet polypyrrole [11] and assuming that the response is linear would yield 0.012 V/m^2 for a 517 mmHg input (e.g., a physiologically relevant pressure condition). Thus the modern materials of ECM must be improved substantially to make these classes of sensors commercially viable for biomedical applications. Specifically improvement in the voltage to pressure response is critical.

In stark contrast we have repeatedly measured ECM voltage response density of 248 V/m^2 while providing a 517 mmHg stimulus using electrolyzed gelatin. The ratio of the 248 V/m^2 response to the 0.012 V/m^2 gives an improvement of over 4-orders of magnitude. One reason gelatin dissolved in water makes an excellent hydrogel for use as the bulk solution in an electrochemical cell (ECC) is due to its charge conducting properties. The charge on the gelatin molecule is primarily due to the side chain carboxyl amino groups [12]. Once dissolved in water, any cation bound to the gelatin molecule dissociates into the water providing a supply of positive charges in addition to the negative charged carboxyl groups throughout the gel. However, the more than 4-order of

magnitude improvement in response cannot solely be accounted for by the improved charge conducting properties of the gelatin system.

The reversible electrode charge transfer kinetics of gelatin has been studied for over a half century [13] with little investigation of the use of gelatin for force sensing despite its low-cost and wide-spread availability. Only recently have some tangentially related investigations been reported where gelatin is being evaluated as a conductor in an ECC [14].

1.4 Summary of Research Goals

The aim of this research project is to investigate an ECC pressure transducer using gelatin hydrogels. Preliminary measurements of enhanced voltage output for a given pressure actuation are exciting, but irregularities in performance based on processing methods suggested that the source of the enhancement stems from impurities or inclusion bodies within the material. Based on our material processing methods we hypothesized that small gaseous bubbles at the electrode are responsible. While the use of an EPT has been investigated for the past 20 years [8,9], no work has been done to examine the effect of bubbles at the electrode. We further hypothesize that this response is suitable for the backbone of sensing element (i.e., linear behavior over a specific range of pressure).

This research will not be building upon the efforts of others, except for the scientific methodology. Instead this research will be ground breaking, starting at the very beginning to provide the foundation for more in-depth studies to follow. The research will be broken down in the following three chapters, with each chapter presented as a standalone paper with the intent to publish each in separate journals. The first of which

will explain the ECM response in the gelatin hydrogel from an electrochemical perspective. The next chapter will correlate the ECM response to the mechanical changes occurring in the gel, building upon the results from the previous chapter. Finally a chapter will present the outcomes from an *in vitro* study intended to demonstrate the efficacy of the EPT for biological use.

2 Electrochemical Analysis of the Gelatin Hydrogel-Aerogel Interface

2.1 Introduction

Interest in developing electrochemical pressure transducers (EPTs) for commercial applications has steadily been increasing over the past two decades [10, 15]. EPTs offer several advantages over tradition integrated circuit-type pressure sensors because the system (1) creates its own voltage without excitation from a power source, (2) is composed almost entirely of deformable "soft" materials, and (3) can be designed to sense pressure in all directions. With this in mind some of the obstacles that need to be overcome in order to make this class of sensor feasible include improving upon the small signal response to pressure, increasing the sensitivity to small pressures, and reducing or compensating for baseline voltage drift.

An EPT is comprised of a hydrated electrically conductive polymer and at least two electrodes. The premise behind the electrochmomechanical (ECM) response is that as the polymer is stressed, the number of charge carriers in the solution changes and the charge on the polymer becomes polarized which results in a measurable voltage potential [10, 15]. Results in the literature tend to model the polymer as a beam and measure the ECM response as a force deflects the beam [10,15]. Taking some of the early results and applying mechanical properties to the gel, the magnitude of the ECM response can be approximated. Preliminary tests from our research demonstrate a 4-order of magnitude improvement in response compared to published values. Irregularities in performance

based on processing methods suggested that the source of the enhancement is impurities or inclusion bodies within the material. Based on our material processing methods we hypothesized that small gaseous bubbles at the electrode are responsible. More significantly, when the number of bubbles is not at a minimum in the gel we find that the inherent noise of the electrochemical cell (ECC) masks all ECM response.

Two fundamental questions that need to be answered are: first, how are the bubbles influencing the response? Secondly, why haven't other researchers reported this effect? The first question will be addressed in this chapter. As for the second question, it is quite difficult to prove a negative result. Revisiting our hypothesis; we will demonstrate using analytical experimentation and systematic variation of bubble number density that the ECM response due to electrolyzed gelatin is directly proportional to the change in surface area of wet dry interface surrounding the generated bubbles.

2.2 Materials

Type A gelatin from porcine skin with 300 bloom strength and 37% formaldehyde in water were obtained from Sigma-Aldrich (St. Louis, MO).

Platinum electrodes were obtained from Gamry Instruments (Warminster, PA).

6061 Aluminum rods were obtained from McMaster-Carr (Elmhurst, IL) and the exposed surfaces were polished with P1200 diamond sandpaper with an average particle size of 15.3 µm.

2.3 Methods

Preparation of Gelatin Hydrogels

Gelatin hydrogel (gel) samples were prepared at 5% and 17.5% concentration by weight in deionized water and were 100% crosslinked based on the theoretical number of crosslinking sites on each gelatin molecule. Concentrations were selected to investigate a more liquid and more rubber like state. Experiments evaluating the viscosity or consistency for the aerogel as a function of dissolved gelatin lead us to select 5% for the less viscous state and 17.5% for the rubbery state. The gel was heated up to 70 ^{o}C which was above the 50 ^{o}C gel-sol transition temperature for 17.5% gelatin [16]. The gel was constantly stirred by a magnetic stirrer until the gelatin was fully dissolved. Through the process of stirring, bubbles were formed from cavitation. Two subsets of samples could then be created: those with a significant bubble number density and those with little or no bubbles at all. To prepare the samples with bubbles formaldehyde was added and stirring continued for 10 additional minutes at a slower rate. The gel was then poured into its desired container at which point it was allowed to cool down to the test temperature. The gel then remained at this temperature for a period of 24 hours. For the samples without bubbles, the gel was exposed to a vacuum which was constantly adjusted to prevent boil over for a period of ten minutes. Formaldehyde was then added and the gel was continually stirred at a slower rate. The gel was then poured into its desired container and a vacuum was then applied for ten minutes, again constantly adjusted to prevent boil over. The vacuum was then removed and the gel was allowed to cool to its test temperature. The gel then remained at this temperature for a period of 24 hours.

Light Transmission through Gel Cured at Atmospheric Pressure and Vacuum

Light transmission measurements were used to validate that exposure to a vacuum reduces the amount of bubbles in the gel. In this process an excess of bubbles were created using cavitation to quantify the effectiveness of this technique. An Ocean Optics USB2000 spectrometer (Dunedin, FL) was used to measure a 580 nm wavelength light transmission through samples of 5% gel prepared at atmospheric pressure and under vacuum. The amount of light transmission through deionized water was subtracted from the amount of light transmission through the gel. There was a 23% increase in the amount of light transmission through gel exposed to a vacuum than gel not exposed to a vacuum with a confidence level of 0.94.

Determination of Effective Gelatin Diameter

The effective diameter of the gelatin molecules in the 5% concentration gel was measured using a Coulter N4Plus particle sizer. Measurements were taken at angles of 90^{o}, 62.2^{o}, 30.2^{o}, and 22.9^{o} for a sample time of 600 seconds. The polydispersion index (PDI) was measured between 0.8 and 1.0 for all samples. A PDI greater than 0.1 indicates that there is a large aspect ratio in the dimension, therefore the measurements at all 4 angles were averaged.

Viscosity Measurement

The viscosity of the 5% concentration gel was measure at 37 ^{o}C using a Bohlin Instruments CVO cone and plate rheometer. The viscosity was measured at an applied shear rate of 0.1 1/s on a 20 mm parallel plate.

Electrolysis

During the preparation of the gelatin hydrogels used to characterized ECM response due to pressure gel containing, bubbles were generated by the process of hydrolysis. These bubbles, unlike those formed by cavitation, have a preferential distribution at the electrode surface. Although response curves from materials containing bubble generated by cavitation were measured, we have chosen not to present the data within the current discussion. Aluminum electrodes were used for each test that electrolysis was performed. The Pourbaix diagram of aluminum [17] at 25 ^{o}C in Figure 2.1 illustrates the potential reactions that can occur at a given applied voltage potential and pH. With the aluminum electrodes, two parallel reactions occur; one for the aluminum and one for the aluminum oxide layer given by Equation 2.1 which corresponds to line 2 in Figure 2.1. Two additional reactions occur involving the water, which result in the generation of hydrogen at the cathode and oxygen at the anode given by Equations 2.2 and 2.3 which correspond to lines a and b respectively in Figure 2.1. Electrolysis was performed on the ECC at 5.0 V for 60 seconds at 25 ^{o}C.

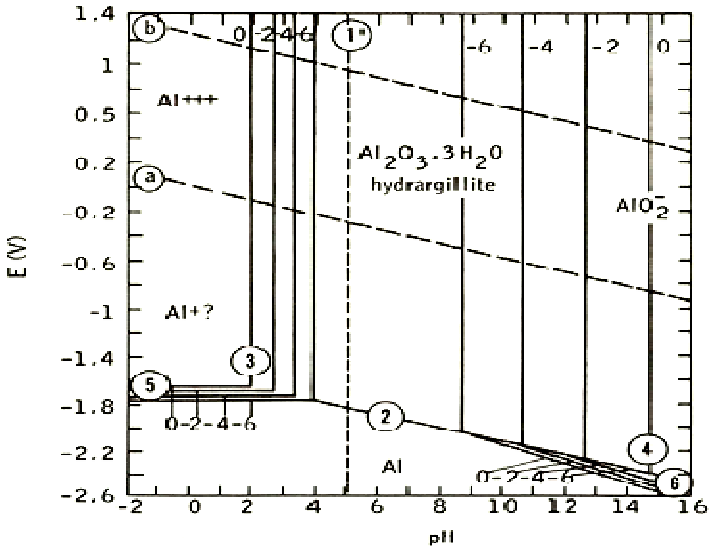

Figure 0.1 – Pourbaix diagram of Aluminum at 25 ^{o}C in water reproduced from [17]. The reversible reactions are indicated by a letter or number enclosed by a circle. The line associated with each of the reactions designates the boundary for the conditions in terms of voltage and pH at which the reaction will occur.

$$2Al + 3H_2O \leftrightarrow Al_2O_3 + 6H^+ + 6e^- \quad 2.1$$

$$2H^+ + 2e^- \leftrightarrow H_2 \quad 2.2$$

$$O_2 + 4H^+ + 4e^- \leftrightarrow 2H_2O \quad 2.3$$

In order to determine the effect of pressurization on the ECC, the galvanic potential must be moved away from equilibrium such that the exchange current density is not zero. This is the sum of the anodic and cathodic current flow. The potential of the ECC will be governed by the Nernst equation [18] given as Equation 2.4, where E is the electric potential, E^o is the standard electrode potential, n is the number of electrons involved in a half cell reaction, and c_j represents the concentration of a species ĵ.

$$E = E^0 + \frac{R \cdot T}{n \cdot F} \cdot (\sum_{ox} \ln c_{\hat{j}} - \sum_{red} \ln c_{\hat{j}}) \quad 2.4$$

If we return to the Pourbaix diagram shown in Figure 2.1 and Equation 2.4, we can see that this potential will be affected by the concentration of Al^{+3} and Al_2O_3 in the solution. This is an oversimplified example, because the potential will be the summation of all reductants and oxidants in the solution. Further, the Nernst equation will also govern the membrane or boundary layer effects in the ECC. This is the concentration of a species in the bulk solution compared to the concentration of the same species at the electrode surface. This indicates that if an electric potential is applied across the electrode to the bulk solution; a concentration gradient for species j will exist according to Equation 2.4.

Electrochemical Impedance Spectroscopy

An electrochemical cell consists of two solid conducting electrodes immersed in a liquid medium containing an electrolyte or charge carriers. Two distinct regions exist; the bulk solution containing the electrolytes and the electric double layer (EDL), which is the interface between the electrolytes and the electrodes characterized by Helmholtz, Gouy, and Chapman [19]. The impedance of the double layer is derived from Fick's second law of diffusion [20] and can account for a significant portion of the total impedance of the cell.

Impedance spectroscopy is a technique used to help gain insight into the electrical properties of an ECC. In the simplest terms, it involves applying a voltage or current at multiple frequencies and then calculating the impedance at each frequency. With the impedance versus frequency (Bode) and imaginary impedance versus real impedance (Nyquist) plots, electrical analytical methods can be used to model the ECC with

electrical components. Once the model has been determined, optimization techniques can then be used to fit the data and determine the values of the electrical components. The accepted model for an ECC using only ideal electrical components is the Randles Circuit [21]. The complete equivalent circuit with the addition of non-linear Warburg impedance is provided by MacDonald [22] and shown in Figure 2.2.

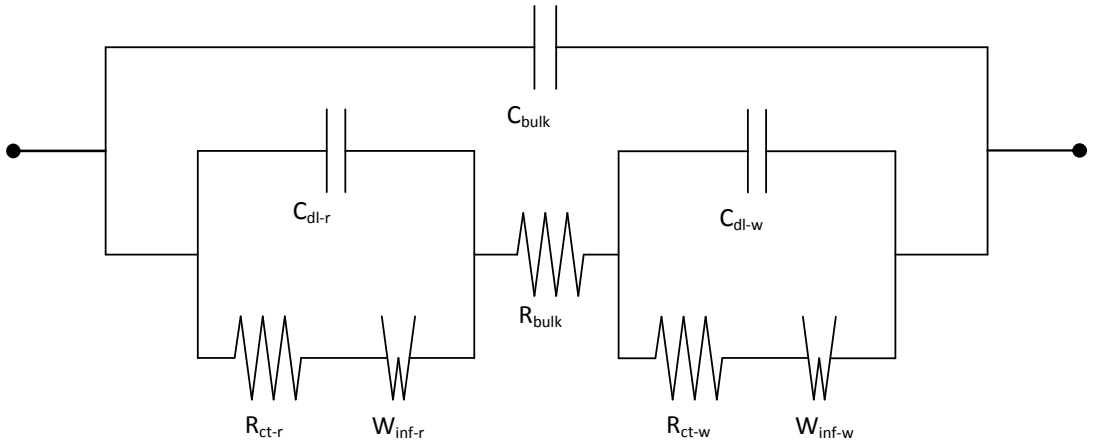

Figure 0.2 – Randles Circuit diagram: C_{bulk} represents the bulk capacitance, C_{dl} represents the double layer capacitance, R_{bulk} represents the bulk resistance, R_{ct} represents the charge transfer resistance and W_{inf} represents the non-linear Warburg impedance. The hyphenated subscript r represents the reference electrode whereas the w represents the working electrode.

Impedance spectroscopy has been used to interpret the electrical properties of electrochemical cells containing polypyrrole in terms of an equivalent circuit comprising ideal electrical components and nonlinear impedance terms [23-25]. The reversible electrode charge transfer kinetics of gelatin, has been studied for over a half century [26] with little published documentation of the use of gelatin for force sensing despite its low-cost and wide-spread availability. However, recent impedance spectroscopy has been used to evaluate the use of gelatin in an ECC as a conductor for industrial applications [14].

The experimental setup for the EIS test comprised a Fisher Scientific heated water bath with the stainless tub making contact with a tin upper enclosure effectively producing a Faraday cage. A glass cell located inside the water bath housed the gel and provided airtight openings for multiple electrodes and a pressurized nitrogen gas line. The electrodes were insulated with Teflon® on all surfaces except for the tip which included 4 mm diameter platinum and 0.125 inch diameter aluminum electrodes. The electrodes were connected to a Gamry Instruments Series G300 potentiostat. A diagram of the test setup is provided in Figure 2.3. Impedance measurements were made at a frequency range from 0.2 Hz to 100 kHz with 30 points taken per decade at a 10 mV AC potential. It has been shown that the basic differential equations that govern the response of the system are linear as long as the stimulus is below the thermal voltage given in Equation 2.4 [27] in which R is the universal gas constant, T is temperature in Kelvin, and F is Faraday's constant. At both 25 and 37 ^{o}C the thermal voltage is approximate 25 mV.

$$V_T \equiv \frac{R \cdot T}{F} \qquad 2.5$$

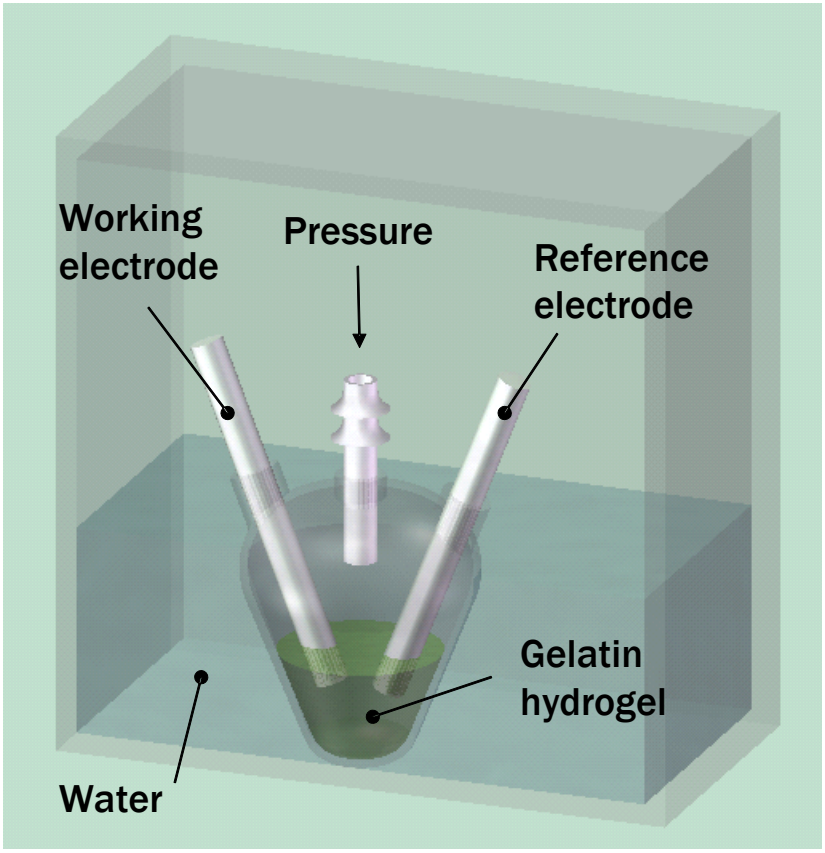

Figure 0.3 – Diagram of EIS test setup. A glass cell is shown in the center of a heated water bath. Two insulated electrodes make contact with the gelatin hydrogel inside the glass cell. A port in the glass cell allows a nitrogen gas supply to pressurize the gel.

EIS was performed on samples at atmospheric pressure. Each test would take approximately fifteen minutes to complete. Next the sample was pressurized to 517 mmHg and EIS was then repeated. After these measurements were taken, the pressure was released and EIS was performed again at atmospheric pressure.

Modeling the Equivalent Circuit

The data taken from the EIS experiments was analyzed using Gamry Instruments 300EIS software. The impedance at each data point consists of a real component, the

resistance and an imaginary component, the reactance along with the corresponding frequency at which it was measured. Referring back to Figure 2.2, the impedance of each of the components in the circuit can be represented by Equations 2.6 – 2.10 where Z is the impedance and the subscript indentifies the component, ω is the frequency, σ is the Warburg coefficient, and j is the square root of negative 1.

$$Z_{Rbulk} = R_{Bulk} \tag{2.6}$$

$$Z_{Rct} = R_{ct} \tag{2.7}$$

$$Z_{Cbulk} = \frac{1}{j \cdot \omega \cdot C_{Bulk}} \tag{2.8}$$

$$Z_{Cdl} = \frac{1}{j \cdot \omega \cdot C_{dl}} \tag{2.9}$$

$$Z_{Winf} = \sigma \cdot \omega^{-\frac{1}{2}} \cdot (1 - j) \tag{2.10}$$

The total impedance at any given frequency is the series parallel combination of the impedance of each of the individual components. For example, for the circuit given in Figure 2.2, the total impedance is given in equation 2.11.

$$Z_{Total} = \frac{\left(\frac{(Z_{Rct-r}+Z_{Winf-r})\cdot Z_{Cdl-r}}{Z_{Rct-r}+Z_{Winf-r}+Z_{Cdl-r}} + Z_{Rbulk} + \frac{(Z_{Rct-w}+Z_{Winf-w})\cdot Z_{Cdl-w}}{Z_{Rct-w}+Z_{Winf-w}+Z_{Cdl-w}}\right)\cdot Z_{Cbulk}}{\frac{(Z_{Rct-r}+Z_{Winf-r})\cdot Z_{Cdl-r}}{Z_{Rct-r}+Z_{Winf-r}+Z_{Cdl-r}} + Z_{Rbulk} + \frac{(Z_{Rct-w}+Z_{Winf-w})\cdot Z_{Cdl-w}}{Z_{Rct-w}+Z_{Winf-w}+Z_{Cdl-w}} + Z_{Cbulk}} \tag{2.11}$$

This equation is the total impedance at each frequency, therefore to determine the individual resistances, capacitances, and Warburg coefficients, this equation must be optimized at each frequency. Fortunately the EIS300 software has the capability to use Simplex based optimization on the dataset, however in order for it to converge on an optimal solution; a reasonable accurate initial guess is required for all of the parameters [28].

Methods for Establishing the Initial Guess

To determine the initial guesses for each of the parameters, the parameters must be calculated based on their basic governing equations. The fundamental equations bulk resistance, bulk capacitance and double layer capacitance are given in Equations 2.12 – 2.14, where l is the spacing between electrodes, μ_g is the electric mobility of gelatin, c_g is the concentration of carboxyl groups in the gelatin [12], this value represents the negative charge conductors, A is the surface area of the electrodes, cf is fringe effects correction factor, ε_o is the permittivity of free space, and ε_r is the dielectric constant with a value of 87 [29]. The equation for the electric mobility of gelatin is derived from the diffusion coefficient of gelatin (D_g); both Equations are given as 2.15 and 2.16 respectively, where q_g is the charge per molecule, k is Boltzmann's constant, η_g is the viscosity of gelatin, and d_g is the effective diameter of a gelatin molecule.

$$R_{Bulk} = \frac{l}{F \cdot \mu_g \cdot c_g \cdot A \cdot cf} \quad 2.12$$

$$C_{Bulk} = \frac{\varepsilon_o \cdot \varepsilon_r \cdot A \cdot cf}{l} \quad 2.13$$

$$C_{dl} = \left(\frac{\varepsilon_o \cdot \varepsilon_r \cdot F^2 \cdot c_g}{R \cdot T}\right)^{\frac{1}{2}} \cdot A \cdot cf \quad 2.14$$

$$\mu_g = \frac{q_g \cdot D_g}{k \cdot T} \quad 2.15$$

$$D_g = \frac{k \cdot T}{3 \cdot \pi \cdot \eta_g \cdot d_g} \quad 2.16$$

The fringe effect is the electric field that is outside the cylindrical space occupied by two parallel separated conductive disks. Typically the electric field is neglected if the ratio of diameter to distance apart is large. For the current setup the ratio is on the order of ¼, so these effects cannot be neglected. Figure 2.4 shows a graphical representation of

the fringe effect. The equation for the correction factor is provided in Equation 2.17 [30], where r is the radius of the electrode and e is base of the natural log.

$$cf = 1 + \left[\frac{2 \cdot l}{\pi \cdot r} \ln \frac{8 \cdot \pi \cdot r}{e \cdot l} + \left(\frac{l}{\pi \cdot r} \ln \frac{l}{8 \cdot \pi \cdot r}\right)^2\right] \quad 2.17$$

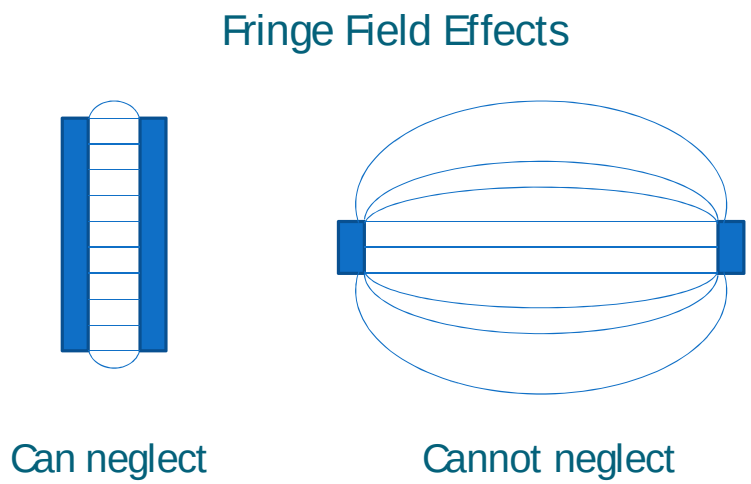

Figure 0.4 – Graphical representation of the fringe effect. The solid rectangles represent electric conductors and the lines between the conductors represent the electric field flux.

After calculating the initial parameters, a sample of 5% concentration gelatin hydrogel is tested using EIS, with two platinum electrodes. This will allow the software to calculate all the parameters in the model. The values of these baseline parameters are close enough in magnitude for the software to obtain an optimum solution for the 17.5% gelatin hydrogel using aluminum electrodes before and after hydrolysis.

Open Circuit Voltage

The simplest potentiostatic test is to measure the open circuit voltage of the ECC. This test involves measuring the voltage across the electrodes at various pressures using a Gamry Instruments Series G300 potentiostat. After electrolyzing the samples, the

samples were left alone for a period of 16 hours for the ECC to reach equilibrium. The samples were then pressurized for ten seconds and then relaxed (ambient pressure) for 10 seconds. This cycle was repeated at increasing pressures of 51.7 mmHg increments up to 517 mmHg and then repeated for another complete cycle up to 517 mmHg. Then the samples were cycled from 0 to 517 mmHg 6 more times.

2.4 Results

A 20 hour test was conducted to evaluate the stability of the OCV after electrolyzing the ECC. This test was performed to determine the period of time after electrolysis that the ECC would reach equilibrium. A plot of the OCV over a period of 20 hours is shown in Figure 2.5.

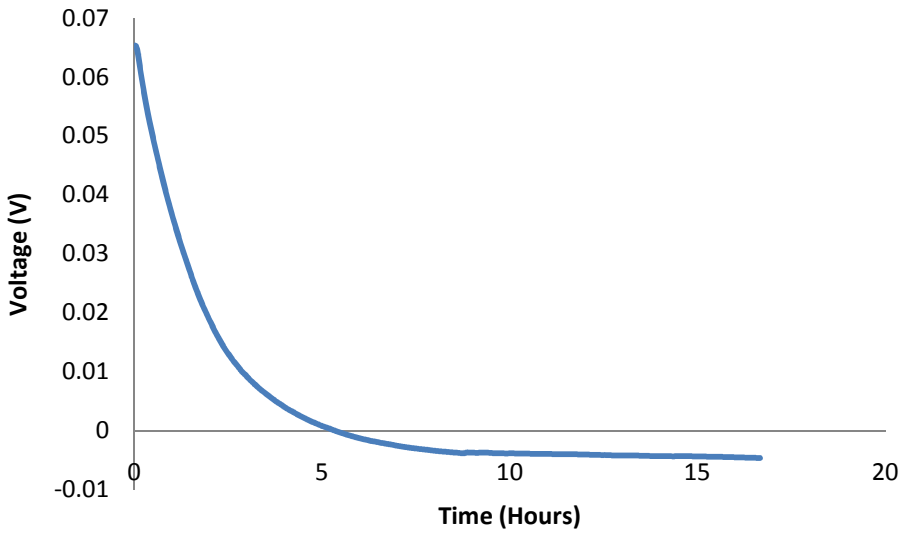

Figure 0.5 – Plot of OCV versus time of an ECC with 17.5% gelatin and two aluminum electrodes at 25 ^{o}C. The x-axis along the bottom of the plot is linear with a range of 0 to 20 hours. The y-axis along the left-hand side of the plot is also linear with a range of -0.01 to 0.07 volts. The raw data for voltage is represented by a blue line.

EIS was performed on a sample to evaluate the model fit for the electrical equivalent circuit of both the Randle's circuit with and without non-linear Warburg terms. The plot of the impedance and phase angle for an ECC with 17.5% gelatin, two aluminum electrodes, pressurized to 517 mmHg at 25 ^{o}C is shown in Figure 2.6. The values for each of the associated circuit elements is given in Table 2.1

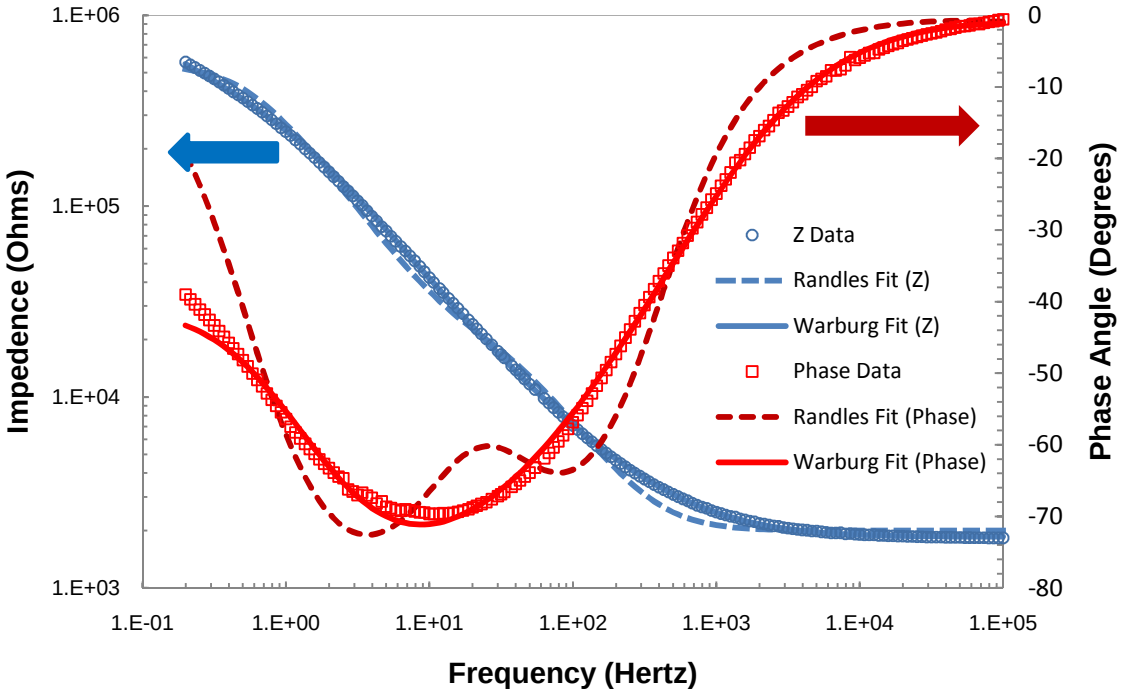

Figure 0.6 – Plot of impedance and phase angle versus frequency of an ECC with 17.5% gelatin, two aluminum electrodes, pressurized to 517 mmHg at 25 ^{o}C. The x-axis along the bottom of the plot is logarithmic with a range of 100 mHz to 100 kHz. The y-axis along the left-hand side of the plot is logarithmic with a range of 1.00 k ohm to 10 M ohm. The y-axis on the right-hand side of the plot is linear with a range of -80^{o} to 20^{o}. The raw data for impedance is represented by open blue circles, while the raw data for phase angle is represented by open red squares. The Randle's circuit model fit is represented by a red dashed-line and a blue dashed-line for the impedance and phase angle respectively. The Randle's circuit with Warburg terms model fit is represented by a red line and a blue line for the impedance and phase angle respectively.

Table 0.1 – Circuit component values with their associate error from Randles Circuit and Randle's Circuit with Warburg terms Model fit.

	Randle's Circuit			Randle's Circuit with Warburg Terms		
Parameter	*Value*	*Error*	*% Error*	*Value*	*Error*	*% Error*
Rbulk (Ω)	2.00E+03	7.678	0.38%	1.85E+03	28.01	1.51%
Cbulk (F)	9.82E-12	9.00E-12	91.69%	7.79E-12	1.44E-11	184.88%
Rct-w (Ω)	1.15E+04	226.8	1.98%	10.16	5.52E+03	54320.87%
Rct-r (Ω)	5.41E+05	4.54E+03	0.84%	2.32E+05	8.15E+03	3.52%
Cdl-w (F)	3.89E-07	4.60E-09	1.18%	7.92E-08	5.38E-07	679.00%
Cdl-r (F)	5.31E-07	3.15E-09	0.59%	5.06E-07	8.49E-09	1.68%
*Wdif-w [S*s^(1/2)]*				9.90E-06	3.45E-07	3.49%
*Wdif-r [S*s^(1/2)]*				2.40E-06	8.89E-08	3.71%
Goodness of Fit	2.14E-02			6.03E-04		

EIS was performed on a 17.5% gelatin sample with two aluminum electrodes at 25 ^{o}C; electrolysis was performed on the sample prior while still in a liquid phase and then the ECC was subject to a vacuum to remove any bubbles that formed on the electrodes. EIS was first performed at 0 mmHg, and then it was repeated on the same sample at 517 mmHg. The plot in Figure 2.7 shows the results from the test. At each frequency there is a pair of samples for both impedance and phase angle, i.e. one data point from 0 mmHg test and one data point from the 517 mmHg test. There is enough overlap at each frequency such that it is difficult to see both sets of the data points. At frequencies less than 3.0 Hz the vertical separation of the data is more apparent.

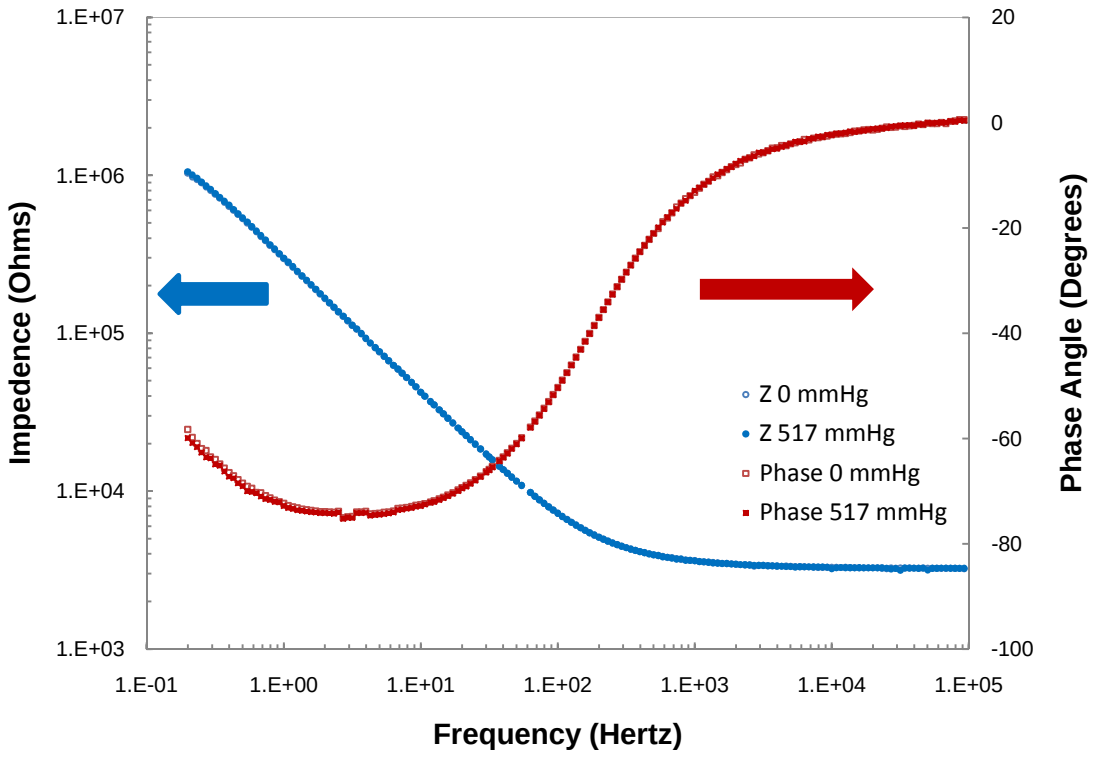

Figure 0.7 – Plot of impedance and phase angle versus frequency of an ECC with 17.5% gelatin, two aluminum electrodes, at 25 ^{o}C. The x-axis along the bottom of the plot is logarithmic with a range of 100 mHz to 100 kHz. The y-axis along the left-hand side of the plot is logarithmic with a range of 1 k ohm to 10 M ohm. The y-axis on the right-hand side of the plot is linear with a range of -100^{o} to 20^{o}. The raw data for impedance is represented by open blue circles and solid blue circles, at pressures of 0 mmHg and 517 mmHg respectively. The raw data for phase angle is represented by open red squares and solid red diamonds, at pressure of 0 mmHg and 517 mmHg respectively.

EIS was performed on a 17.5% gelatin sample with two aluminum electrodes at 25 ^{o}C; electrolysis was performed on the sample prior to testing. EIS was first performed at 0 mmHg, then it was repeated on the same sample at 517 mmHg, and finally it was repeated at 0 mmHg. The plot in Figure 2.8 shows the results from the test. At the frequency range of 1.0 Hz to 100 Hz it can be seen that was phase angle increases in the negative direction after applying a 517 mmHg stimulus, and approaches the original values when the stimulus is removed. For the impedance it can been seen over the entire

bandwidth that the impedance decreases after receiving a 517 mmHg stimulus and returns to an intermediate value between the original 0 mmHg impedance and 517 mmHg impedance after the 517 mmHg stimulus is removed. The data shown in Table 2.2, shows the value of the Randle's circuit parameters for each set of data: 0 mmHg, 517 mmHg, and then 0 mmHg.

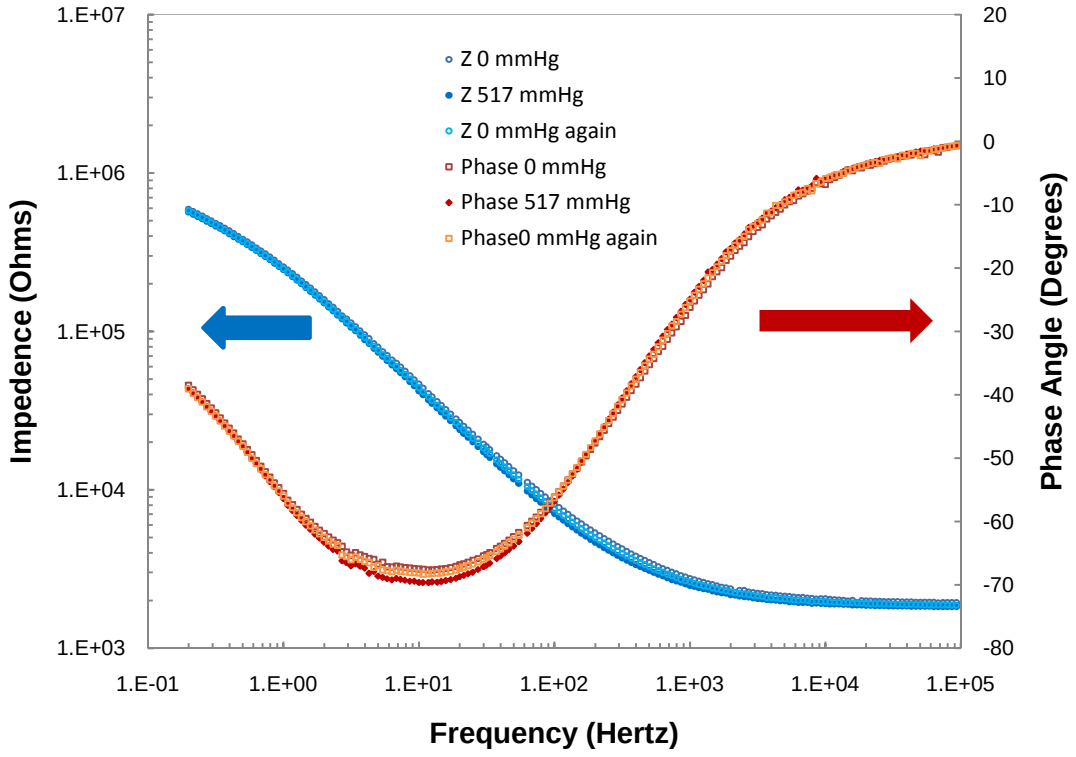

Figure 0.8 – Plot of impedance and phase angle versus frequency of an ECC with 17.5% gelatin, two aluminum electrodes, at 25 ^{o}C. The x-axis along the bottom of the plot is logarithmic with a range of 100.0 mHz to 100 kHz. The y-axis along the left-hand side of the plot is logarithmic with a range of 1 k ohm to 10 M ohm. The y-axis on the tight-hand side of the plot is linear with a range of -80^{o} to 20^{o}. The raw data for impedance is represented by open dark blue circles, solid blue circles and open light blue circles, at pressure of 0 mmHg, 517 mmHg, and then 0 mmHg respectively. The raw data for phase angle is represented by open red squares, solid red diamonds, and open orange squares, at pressure of 0 mmHg, 517 mmHg, and 0 mmHg respectively.

Table 0.2 – Circuit component values with their associate error from the Randle's Circuit model fit for each set of data plotted in Figure 2.8.

		error		*error*		*error*	*Δ 0-517mmHg*	*Δ% 0-517mmHg*
Pressure (mmHg)	**0**		**517**		**517**			
R bulk (Ω)	**2.13E+03**	8.258	**2.00E+03**	7.678	**2.06E+03**	7.933	**1.31E+02**	**6.16%**
R ct-w (Ω)	**1.30E+04**	2.27E+02	**1.15E+04**	2.27E+02	**1.25E+04**	2.31E+02	**1.48E+03**	**11.42%**
R ct-r (Ω)	**5.51E+05**	4.57E+03	**5.41E+05**	4.54E+03	**5.47E+05**	4.60E+03	**9.60E+03**	**1.74%**
C bulk (F)	**9.51E-12**	8.41E-12	**9.82E-12**	9.00E-12	**9.50E-12**	8.68E-12	**3.10E-13**	**3.26%**
C dl-w (F)	**3.07E-07**	3.37E-09	**3.89E-07**	4.60E-09	**3.45E-07**	3.87E-09	**8.17E-08**	**26.61%**
C dl-r (F)	**5.01E-07**	2.98E-09	**5.31E-07**	3.15E-09	**5.23E-07**	3.12E-09	**2.99E-08**	**5.97%**

The open circuit voltage (OCV) was measured on a 17.5% gelatin sample with two aluminum electrodes at 25 C; electrolysis was performed on the sample prior to testing. The sample was pressurized at approximately 57.1 mmHg, held for 10 seconds and then released. This process was repeated with increasing pressures of approximately 51.7 mmHg for a total of ten times, and then the entire pressurization cycle was repeated again. Finally the ECC was pressurized to approximately 517 mmHg seven more times. While the target pressure was applied at 51.7 mmHg intervals, the precise pressure measured to the nearest 0.5 mmHg was recorded separately. The plot in Figure 2.9 shows the OCV results as a function of time. While the plot in Figure 2.10 shows the change in voltage as a function of the change in pressure.

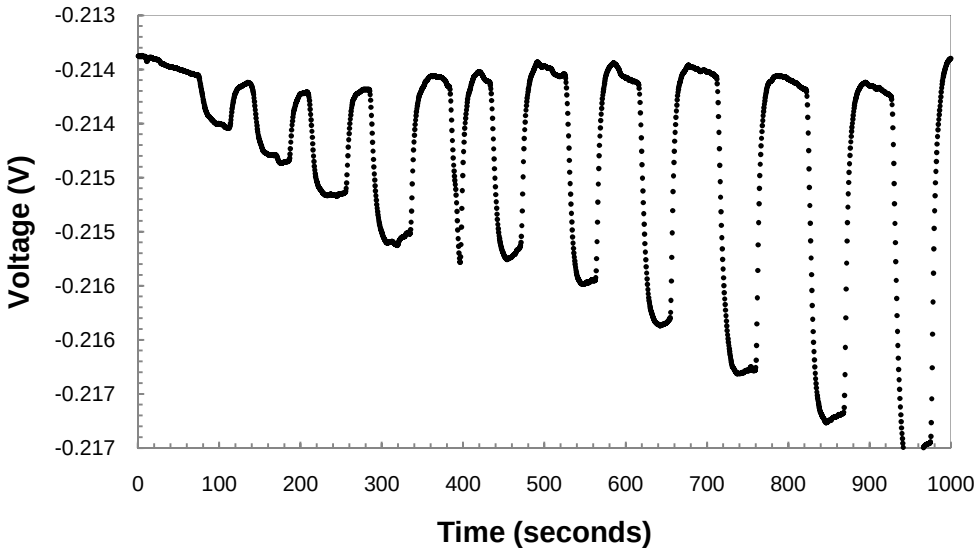

Figure 0.9 – Plot of OCV versus time of an ECC with 17.5% gelatin, two aluminum electrodes, at 25 ^{o}C. The x-axis at the bottom of the plot has a range of 0 seconds to 1000 seconds. The y-axis on the right-hand side of the plot has a range of -217 mV to -213 mV, the value of the pressure impulse is not shown in this plot.

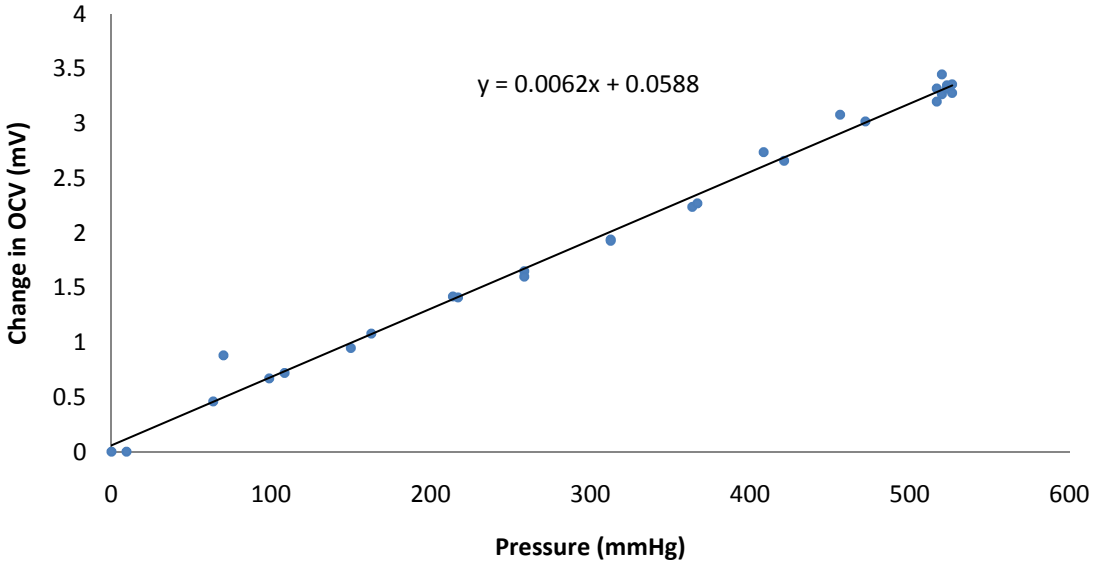

Figure 0.10 – Plot of the change in OCV versus the change in applied pressure in an ECC with 17.5% gelatin, two aluminum electrodes, at 25 ^{o}C. The x-axis at the bottom of the plot has a range of 0 to 600 mmHg. The y-axis on the left-hand side of the plot has a range of 0 mV to 4 mV. Each solid blue circle represents the raw data. A least squared linear regression line is plotted through the data and is the reported on the plot along with the coefficient of determination denoted R^2.

2.5 Discussion

Several interesting findings became apparent in the results. Using the data for the model fit shown in Figure 2.6, it can be seen that the Randle's circuit plus Warburg terms provides an excellent fit with the impedance curve going through every data point, and the phase angle curve closely following the data with small deviations between 3 and 11 Hz and frequencies less than .5 Hz. The Randle's circuit without Warburg terms provides a reasonable fit for the impedance curve with slight deviations along the curve. The phase angle curve did capture the general shape of the data, but had large deviations from the actual values. This does show that the Randle's circuit plus Warburg terms does model the ECC better than the Randle's circuit alone with a goodness of fit of 0.0006 compared to 0.021 respectively, however a closer look at the values in Table 2.1 will demonstrate that the Randle's circuit without Warburg terms provides a more useful tool for analysis.

The error that is reported is a range that describes the parameter sensitivity. This is the range of values that the circuit parameter can take on to achieve the same goodness of fit, another way to put it is that the larger the error, the more optimal solutions can fit the data. So even though the goodness of fit for the Randle's circuit with Warburg terms is two orders of magnitude smaller than the Randle's circuit without Warburg terms, there is more variability in some of the parameters. Looking at the Randle's circuit all of the errors are less than 2% except for the bulk capacitance at 92%. The value of the bulk capacitance can fall between approximately 5 and 15 pF. With a capacitance this small it has very little effect on the impedance of the circuit except at high frequencies, even then the effect is negligible. Now turning to the Randle's circuit with Warburg terms, the

amount or variability at the working electrode is large. The charge transfer resistance has an error of 54,320% and the double layer capacitance has an error of 679%. The aim of this study is to investigate the effects at the electrode interface and renders the use of the Randle's circuit plus Warburg terms of little value. Therefore, the analysis that follows in this discussion will use the Randle's circuit parameters.

Comparing the plots in Figures 2.11 and 2.12, it is obvious from visual inspection that that the impedance of an ECC is affected by pressurization when bubbles are present after electrolysis. This is the only variable that differed from the two tests. A closer analysis is needed to show that this occurs at the electrode interface and not in the bulk solution of the ECC.

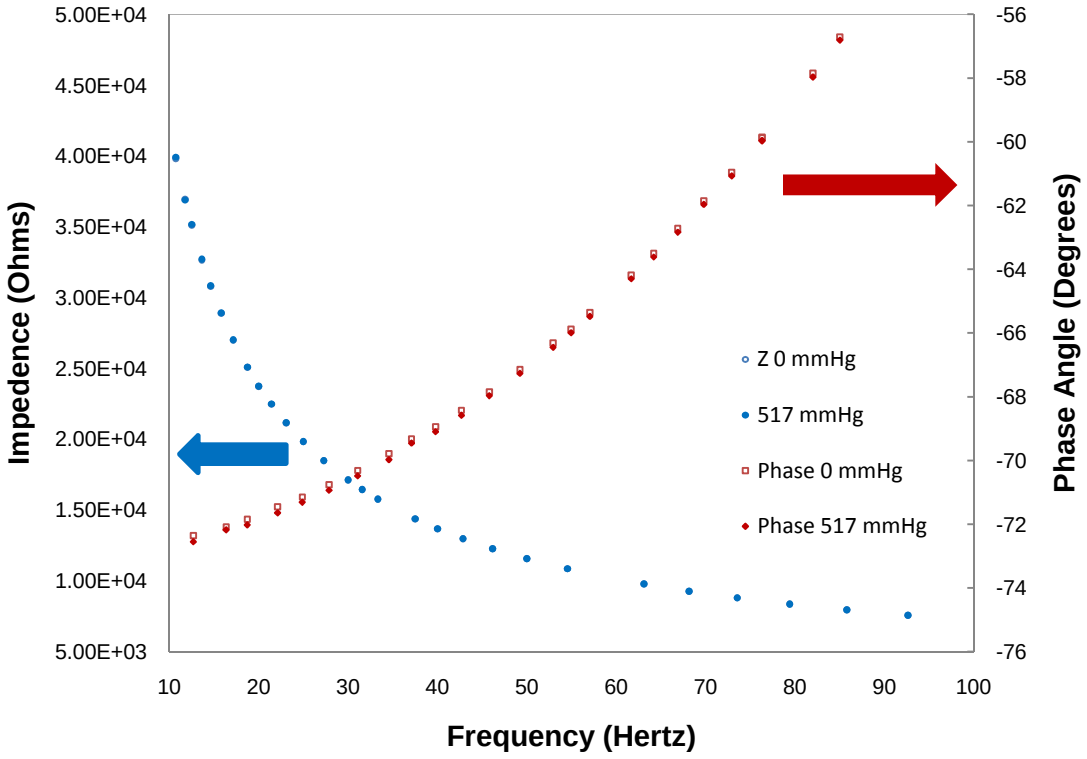

Figure 0.11 – Plot of impedance and phase angle from Figure 2.7 with a frequency range of 10 to 100 Hz.

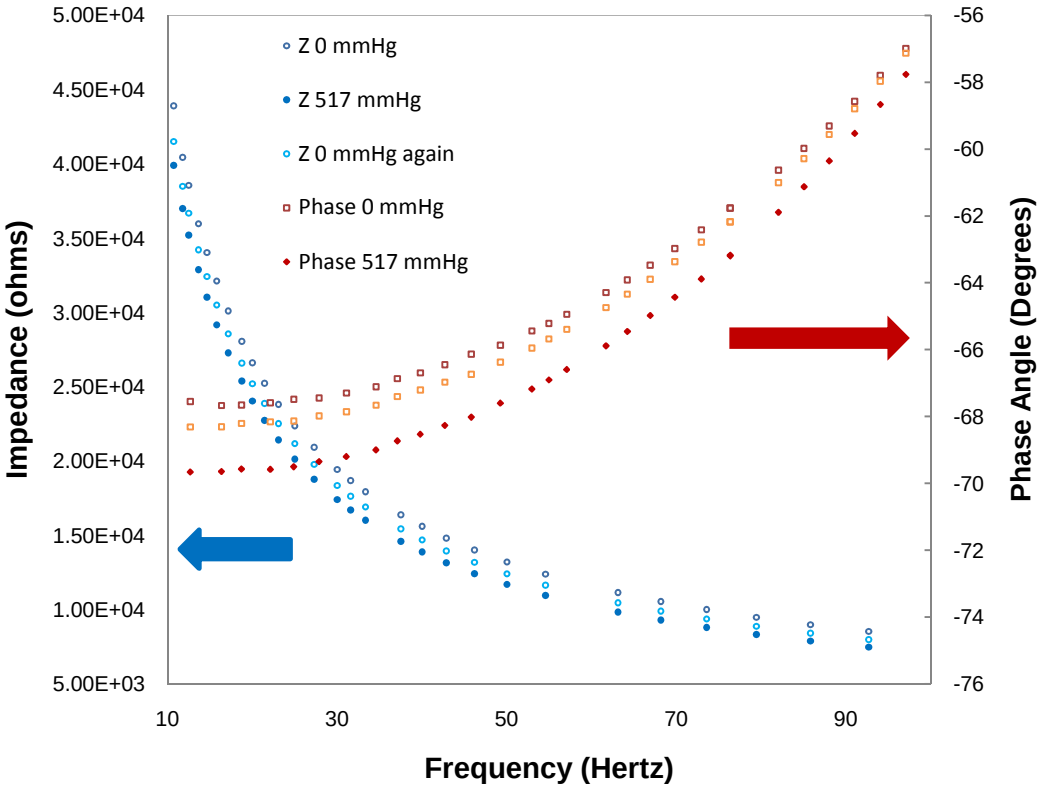

Figure 0.12 – Plot of impedance and phase angle from Figure 2.8 with a frequency range of 10 to 100 Hz.

Looking at Table 2.2, the far right two columns show the change in the parameters as the ECC is pressurized from 0 to 517 mmHg, and the percent change that occurs. Using Equation 2.18 the change in resistive elements at the both electrode interfaces as a percentage of the change in total resistance can be computed to be 98.33%. Using Equation 2.19 the change in capacitive elements at the both electrode interfaces as a percentage of the change in total capacitance is computed to be 100%. Thus more than 98% of the change in resistance and capacitance of the entire system is captured by the small region at the electrode interface, confirming that the ECM response to pressure is an interfacial effect.

$$\frac{R_{ct-w,\ \Delta 0-10\ psi} + R_{ct-r,\ \Delta 0-10\ psi}}{R_{ct-w,\ \Delta 0-10\ psi} + R_{ct-r,\ \Delta 0-10\ psi} + R_{bulk,\ \Delta 0-10\ psi}} \cong 98.83\% \quad 2.18$$

$$\frac{C_{dl-w,\ \Delta 0-10\ psi} + C_{dl-r,\ \Delta 0-10\ psi}}{C_{dl-w,\ \Delta 0-10\ psi} + C_{dl-r,\ \Delta 0-10\ psi} + C_{bulk,\ \Delta 0-10\ psi}} \cong 100\% \quad 2.19$$

Further we can show that the interfacial response is due to a change in surface area of the electrode. By examining the dominate electrochemistry at the interface. Referring back to Equation 2.14, the double layer capacitance C_{dl} can be rewritten in terms of the of the thickness of the double layer which is denoted by the Debye length $l_{D,}$ given in Equation 2.20. The charge transfer resistance is given by Equation 2.21, in which i represents the exchange current.

$$C_{dl} = \frac{\varepsilon \cdot \varepsilon_o \cdot A}{l_D} \quad 2.20$$

$$R_{ct} = \frac{R \cdot T \cdot A}{n \cdot F \cdot i} \quad 2.21$$

Derivation of the capacitive double layer equation reveals three potential variables that could change to increase capacitance as pressure increases. First, the dielectric constant of the water ε could increase. This scenario is unlikely because the dielectric constant for water at 25 ^{o}C is approximately 82, and inside the EDL it was found to be approximately 4.5 due to the alignment of the molecules [31]. In order for the values to change, the electric field would have to be removed, and the electric field is inherent inside an EDL. Secondly, the Debye length, which is the thickness of the EDL could decrease, but this is a function of the ionic concentration [32]. It is true that the ionic concentration does change due to the polarization of the electrodes referring back to the

Nernst equation in Equation 2.4, but as will be shown by revisiting Figure 2.9, this is a much slower process. Finally, the surface area of the interface could increase, which is plausible due to the changes in geometry of the air bubbles as they compress.

By investigating the charge transfer resistance, only the current exchange density is a variable. In order for this to change, either the exchange current, which is also driven by the ionic concentration, would have to change or the area would have to increase. As with the reasoning for the change in Debye length, this occurs at a much slower rate. Our hypothesis is that the surface area increases due to the pressurization of air bubbles at the interface. Figure 2.13 is close-up of the plot given in Figure 2.9 with one cyclic pressurization enlarged for illustration. Each time the ECC is pressurized, there is a noticeable change in voltage, illustrated by dE/dA in Figure 2.13. Following the pressurization, there is noticeable drift denoted by dE/d[c] in Figure 2.13. Referring back to the Nernst equation given by Equation 2.4, if there is a change in voltage, the only variables that can change to allow the equation to maintain equality are the temperature and the concentrations of oxidants and reductants. The temperature is held constant, so this means that the concentrations in the solution are changing to establish a new equilibrium in the solution. This is also why the drift continues after the pressurization, the change in voltage is much smaller compared to the initial change, and from visual inspection appears to take the form of logarithmic decay behavior.

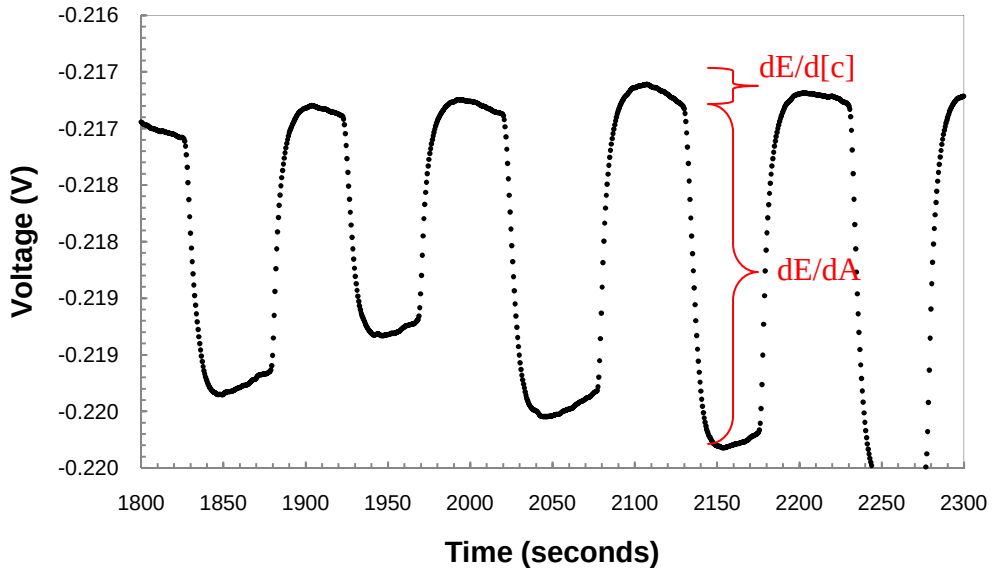

Figure 0.13 – Plot of OCV versus time of an ECC with 17.5% gelatin, two aluminum electrodes, at 25 ^{o}C. The x-axis at the bottom of the plot has a range of 1800 seconds to 2300 seconds. The y-axis on the right-hand side of the plot has a range of -220 mV to -216.0 mV the value of the pressure impulse is not shown in this plot.

2.6 Conclusion

A new material system was established raising the voltage response density for ECM systems by 4-orders of magnitude. Additionally, this investigation definitively shows that an ECM response occurs in an ECC only when bubbles are present. This response has been shown through EIS to occur at the electrode interface, and not in the bulk solution. Through derivation of the governing electrochemical equations of the EDL, it was shown that this response is due to a change in the surface area of the electrode.

Further studies will be needed to show the mechanical relationship of a deformed bubble correlates to the ECM measured. The results show a linear relationship between the ECM and pressurization for the range of 0 to 517 mmHg. To prove that the surface

area is responsible for this effect and to help support our hypothesis, a change in electrode surface area must also be linear for that range under the same conditions.

3 Mechanical Analysis of the Gelatin Hydrogel-Aerogel Interface

3.1 Introduction

The previous work outlined in Chapter 2 predicted that the change in electrode surface area as a result of pressurization was the dominate mechanism governing the ECM response for pressures in the range of 0 to 517 mmHg. Further, the work presented experimental data that showed a linear relationship between ECM response and pressure within the same range. As a consequence of these experimental and analytical observations there must be a linear relationship between in the electrode surface area and applied pressure for the aforementioned pressure range. Moreover, the bubbles generating the enhanced ECM response must participate in this surface area change directly.

For an ECC with bubbles at the electrode, two potential scenarios could produce a change in surface area with pressurization. The first scenario shown in Figure 3.1 A, would include having a solid electrode partially in contact with a bubble and partially in contact with a liquid or gel. As the ECC is pressurized, the single phase gas bubble compresses, effectively reducing its radius; thereby increasing the surface area of liquid or gel in contact with the solid. The second scenario shown in Figure 3.1 B, assumes that the bubble surface area in contact with the solid is fixed, and that pressurization of the ECC would decrease the surface area of the bubble in contact with the liquid or gel. In order for this scenario to be valid, the bubble would have to modeled as an aerogel

instead of a single gas phase, because a conductive matrix would be needed to move charge from the electrode to the liquid interface.

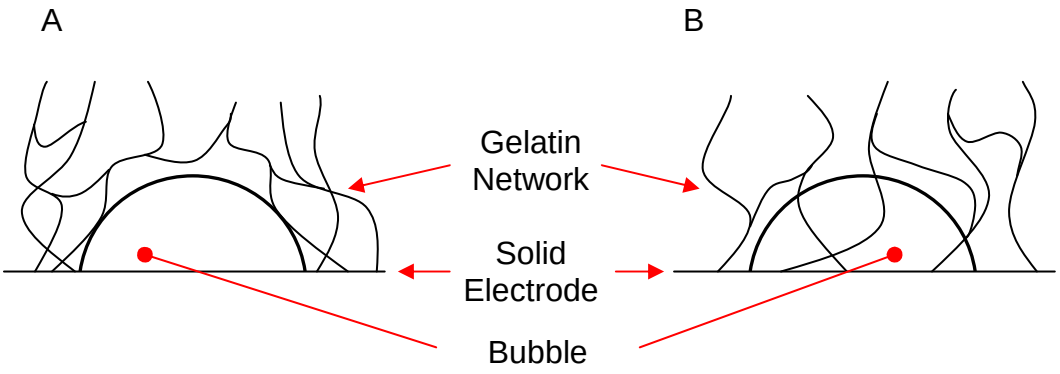

Figure 3.1 – Illustrative representation of a bubble on the electrode surface in a gelatin hydrogel. The first scenario depicted in 3.1 A, shows the bubble displacing the volume of liquid between the gelatin network, whereas 3.1 B, shows the bubble displacing the volume in and around the gelatin network forming an aerogel.

Gas bubble deformation studies have been particularly important for cavitation erosion near ship propellers [33], radioactive waste storage [34], and protein foam production [35]. From these efforts it is well accepted that single phase gas bubbles in a stagnant fluid can be modeled as spheres before and after deformation in a uniform pressure field [35-36]. The Young-Laplace equation [37] describes the pressure in a bubble surrounded by a fluid (Equation 3.1) where P_b is the gas pressure of the bubble, P is the applied pressure, γ is the surface tension, and R_b is the bubble radius.

$$P_b = P + \frac{2 \cdot \gamma}{R_b} \qquad 3.1$$

From equation 3.1 some insight can be gained on how the radius of the bubble changes with pressure. This suggests an inverse but linear relationship with the radius.

However it is difficult to extrapolate this relationship to the change in surface area of the electrode for the case where the bubble contact area is not fixed because we do not know what the position of the bubble changes in relation to the electrode. It also assumes no change in shape as a result of interacting with the electrode surface, and that the bubble acts purely as a gas thus does not contain any liquid or solid structure nor does it change phase during pressurization.

However, the bubbles generated in the process described in chapter 2 may not only consist of a gas, but of a porous solid structure from the crosslinked network. In aerogels the liquid phase of the gel is replaced with a gaseous phase leaving the original porous network. The first aerogels were created using supercritical fluid extraction for thermal insulation and the porous network frequently collapsed [38], because the porous material had weak compressive strength. This is collapse does not necessarily occur in more modern materials especially those possessing suitable independent strength like those established by crosslinked polymer networks.

While there are limited studies that have been performed on protein aerogels [39], investigation on the electrical properties of protein aerogels are absent from the literature. The closest relevant work is on electrochemical applications of aerogels exist specifically for use as batteries and capacitors [40]. For batteries, the most common aerogel electrodes are the oxides of vanadium [41], manganese [42], and molybdenum [43]. For capacitors, carbon has often been studied due to its high conductivity [44-47]. Gelatin aerogels share similar characteristic of the previously mentioned electrode materials in that it consists of a highly connected conductive matrix, with large specific pore volumes. Based on these characteristics, gelatin aerogels are a viable electrode material. It is

important to note that in this case the electrode surface will no longer be the physical metal surface but extended to the surface at the gas liquid interface where the aerogel ends and the traditional gel system begins.

We can gain insight into how the aerogel surface varies as function of pressure by understanding the relationship between pressure and volume. Previous investigators have shown that the Young's modulus of an aerogel obeys a power law relationship as a function of its density given by Equation 3.2, where E_g is the Young's modulus of the aerogel, ρ is the density and E_x and m are constants [48,49]. Subsequently a power law model for pressure and volume has been derived based on the bulk modulus of the aerogel given in Equation 3.3, where P_o is the initial pressure, K_o is the initial bulk modulus, V_o is the initial volume, and V is the final volume [50]. The non-dimensional constant m approximates length to the third power and typical values for aerogels are between 3.0 and 3.5 [50], surface area is the derivative of the volume term and would be described by m-1.

$$E_g = E_x \cdot \rho^m \tag{3.2}$$

$$P = P_o + \frac{K_o}{m} \cdot \left[\left(\frac{V_o}{V}\right)^m - 1\right] \tag{3.3}$$

Neither of the scenarios can be conclusively linked the linear behavior in surface area suggested by chapter 2. Further it is clear that too many unknowns exist in the analytical models of this system to definitively determine the mechanism for bubble interaction with the electrode causing the observed EMC response. Thus the work in this chapter will experimentally explore the effect of pressure on the bubble in gelatin hydrogel in an effort to determine whether the change in surface area is due to a change

in surface area of the liquid-solid interface, or a change in surface area of the aerogel-liquid interface. This chapter will also build upon the conclusions of the previous chapter to show that for a pressure range of 0 to 517 mmHg the change in surface area is linearly related to the change in applied pressure.

3.2 Materials

Type A gelatin from porcine skin with 300 bloom strength and 37% formaldehyde in water were obtained from Sigma-Aldrich (St. Louis, MO).

6061 Aluminum rods and Loctite® 401 cyanoacrylate adhesive were obtained from McMaster-Carr (Elmhurst, IL).

3-1765 Silicon conformal coating was obtained from Dow Corning Corporation (Midland, MI).

3.3 Methods

Experimental Setup

The test setup consisted of a modified cuvette that allowed microscopic imaging to be performed concomitantly with pressurization. The cuvette was modified by drilling two holes at the bottom to allow the insertion of two aluminum rods. Part of the rods extends inward inside the cuvette and a portion of the rods extends outside the cuvette through the bottom to make electrical contact with measuring equipment. The upper portion of each rod was first coated with cyanoacrylate and then with the silicon conformal coating after drying to prevent the sides of the aluminum rod from making contact with the gel. The flat surface at the top of the rod was polished down to remove

the protective coating before insertion into the cuvette. A gelatin hydrogel was added to the cuvette to create the ECC. Silicon tubing was glued to the top of the cuvette and attached to a Welch Allen inflatable bulb and aneroid gauge.

Preparation of Gelatin Hydrogels

Gelatin hydrogel (gel) samples were prepared at 17.5% concentrations by weight in deionized water and were 100% crosslinked based on the theoretical number of crosslinking sites on each gelatin molecule. The gel was heated up to 70 °C while being constantly stirred by a magnetic stirrer until the gelatin was fully dissolved. Through the process of stirring, bubbles were formed from cavitation. Two subsets of samples could then be created: those with a high number density of bubbles and those near negligible number density. To prepare the samples with bubbles formaldehyde was added and stirring continued for 10 additional minutes at a slower rate. The gel was then poured into its desired container at which point it was allowed to cool down to the test temperature. The gel then remained at this temperature for a period of 24 hours. For the samples without bubbles, the gel was exposed to a vacuum which was constantly adjusted to prevent boil over for a period of ten minutes. Formaldehyde was then added and the gel was continually stirred at a slower rate. The gel was then poured into its desired container and a vacuum was then applied for ten minutes, again constantly adjusted to prevent boil over. The vacuum was then removed and the gel was allowed to cool to its test temperature. The gel then remained at this temperature for a period of 24 hours. For the bubble stability test, two samples were used; gel with bubbles generated by cavitation and gel with bubbles created by electrolyzing the cell with 5.0 V for 1 minute. For

microscopic imaging electrolysis was performed on the ECC at 5.0 V until one large bubble covered each of the electrodes.

Bubble Stability

Gel was poured into a flat-bottomed 5 mL glass beaker. The beaker was equipped with a rubber stopper having two parallel aluminum electrodes and a purge hole. The bottom surface of each electrode was flush with the bottom surface of the rubber stopper. The rubber stopper was pressed into the gel before curing such that all the air was evacuated through the purge hole. Imagines were then taken of the surface of the electrodes for each of the samples using a DuncanTech DT1100 camera periodically over 5 days.

Imagery

An Olympus BX51M microscope was used to take digital photographs of the cuvette during pressurization. The cuvette was mounted to the stage of the microscope to prevent moving and a 5x objective lenses was used in conjunction with a 10x ocular lens. The cuvette was pressurized at increasing intervals of 20 mmHg from 0 to 300 mmHg and at each pressure an 8-bit color micrograph was taken. Single frequency impedance measurements were taken of the same sample while in the current setup at 500 Hz. The pressurization was repeated from 0 to 300 mmHg.

Image Analysis

The image analysis was conducted using MathWorks™ (Natick, MA) Matlab image processing toolbox. The brightness and contrast of each image was enhanced based on an algorithm that calculates the distribution of luminosity intensities for each pixel and shifts the curve such that the average luminosity intensity of the curve is moved to the median intensity value of 128. Figure 3.2 A and B show the original and enhanced micrographs taken of the bubble at 0 mmHg. Next the images were converted to black and white using an algorithm that replaces all intensities under a predetermined cutoff value with 0 and intensities over that value to 255. The cutoff value was chosen to capture the outer edge of the bubble and was applied to each of the images. Following the black and white conversion, the images were manually touched up to reduce dithering artifacts that appear away from the edge of the bubble interface. Figure 3.2 C shows the touched up black and white micrograph or the bubble at 0 mmHg. Finally an algorithm was applied to create matrix of the coordinates of the edge between the black and white pixels. Figure 3.2 D shows the highlighted edge, superimposed on the enhanced image.

The images captured are a quarter circle of the front view projection of the hemispherical bubble. In order to calculate the area and volume for each bubble, an assumption was made that the bubble had radial symmetry. The matrix of coordinates for the bubble edge in each image was not 1:1; some of the boundaries had vertical edges that resulted in multiple y-values at a particular x-value; these values were averaged to allow for area and volume calculations. The area of each bubble A_s was calculated by summing the external area of concentric cylinders, with the height of each cylinder

defined by the hypotenuse of adjacent points as given in Equation 3.4, where x_i is the x-coordinate, x_{max} is the x-coordinate at the axis, and y_i is the y-coordinate. The volume was of each bubble, V, was calculated by summing the volume of concentric cylindrical rings above the electrode surface as given in Equation 3.5, where y_{min} is the vertical position of the top of the electrode.

$$A_s = 2 \cdot \pi \cdot \sum (x_{max} - x_i) \cdot [(y_{i+1} - y_i)^2 + 1]^{\frac{1}{2}} \quad 3.4$$

$$V = \pi \cdot \sum \left(\frac{y_i}{2} + \frac{y_{i+1}}{2} - y_{min} \right) \cdot [(x_{max} - x_i)^2 - (x_{max} - x_{i+1})] \quad 3.5$$

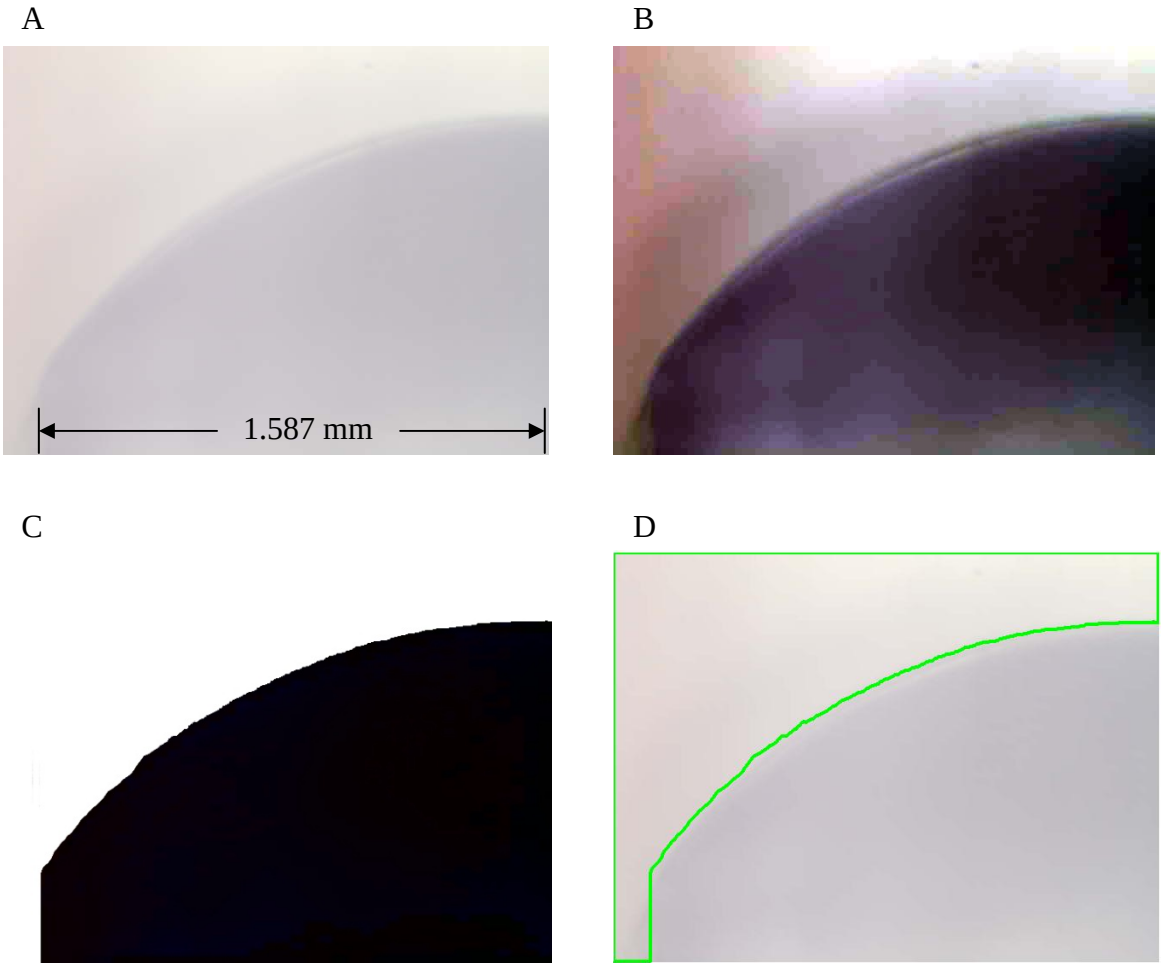

Figure 3.2 – Front view micrographs of a bubble on top of an anode in an ECC, all images were taken at 25 ^{o}C and 0 mmHg. Image A is the original micrograph, Image B is an enhanced image of the original micrograph, Image C is the black and white conversion of the enhanced image, and Image D is the original micrograph with the edge boundary superimposed on it.

3.4 Results

Figure 3.3 shows the degeneration of the oxygen bubbles on the anode over a period of 4 days. Figure 3.4 shows the hydrogen bubbles on the cathode over a period of 4 hours. Air bubbles generated by cavitation are shown in Figure 3.5 over a period of 5 days.

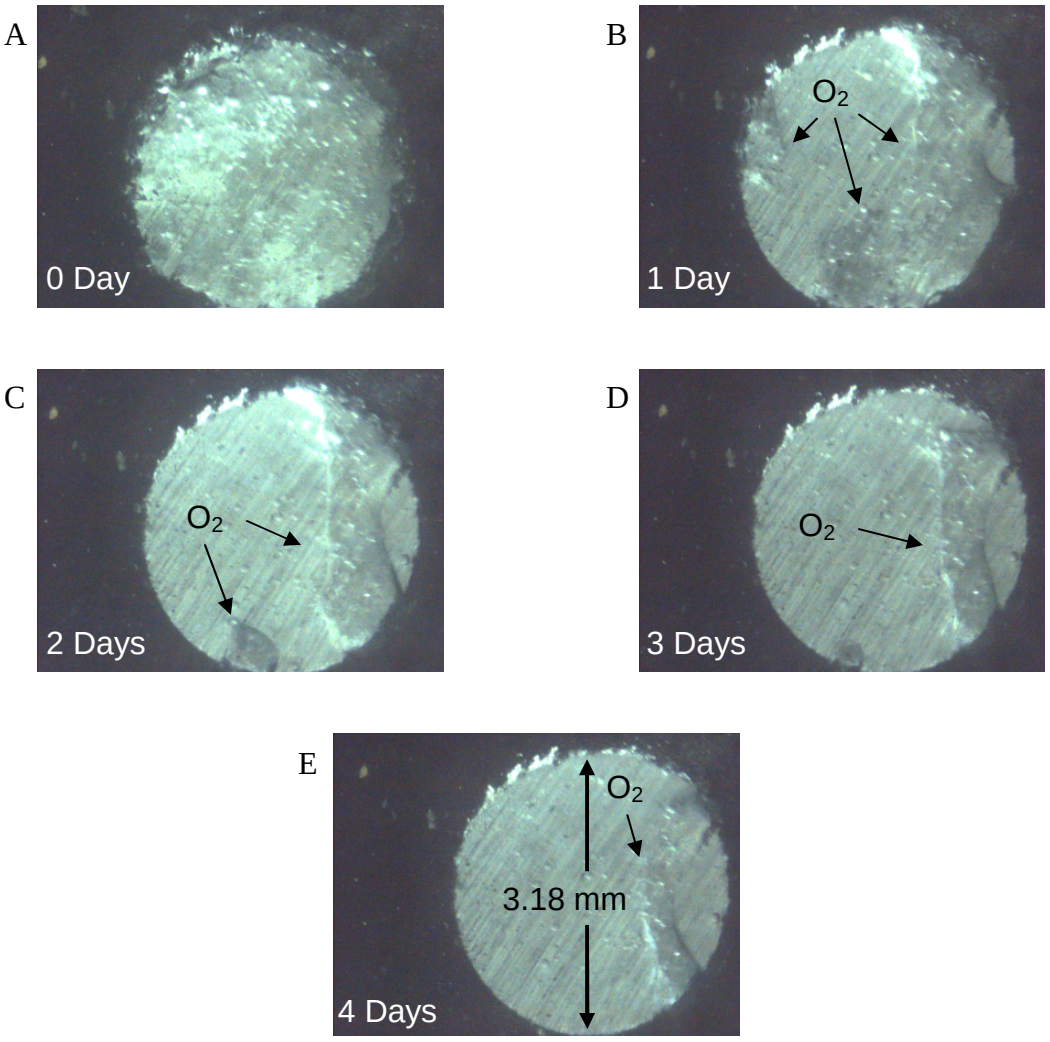

Figure 3.3 – Top view photographs of oxygen bubbles on the anode surface taken over a period of 4 days.

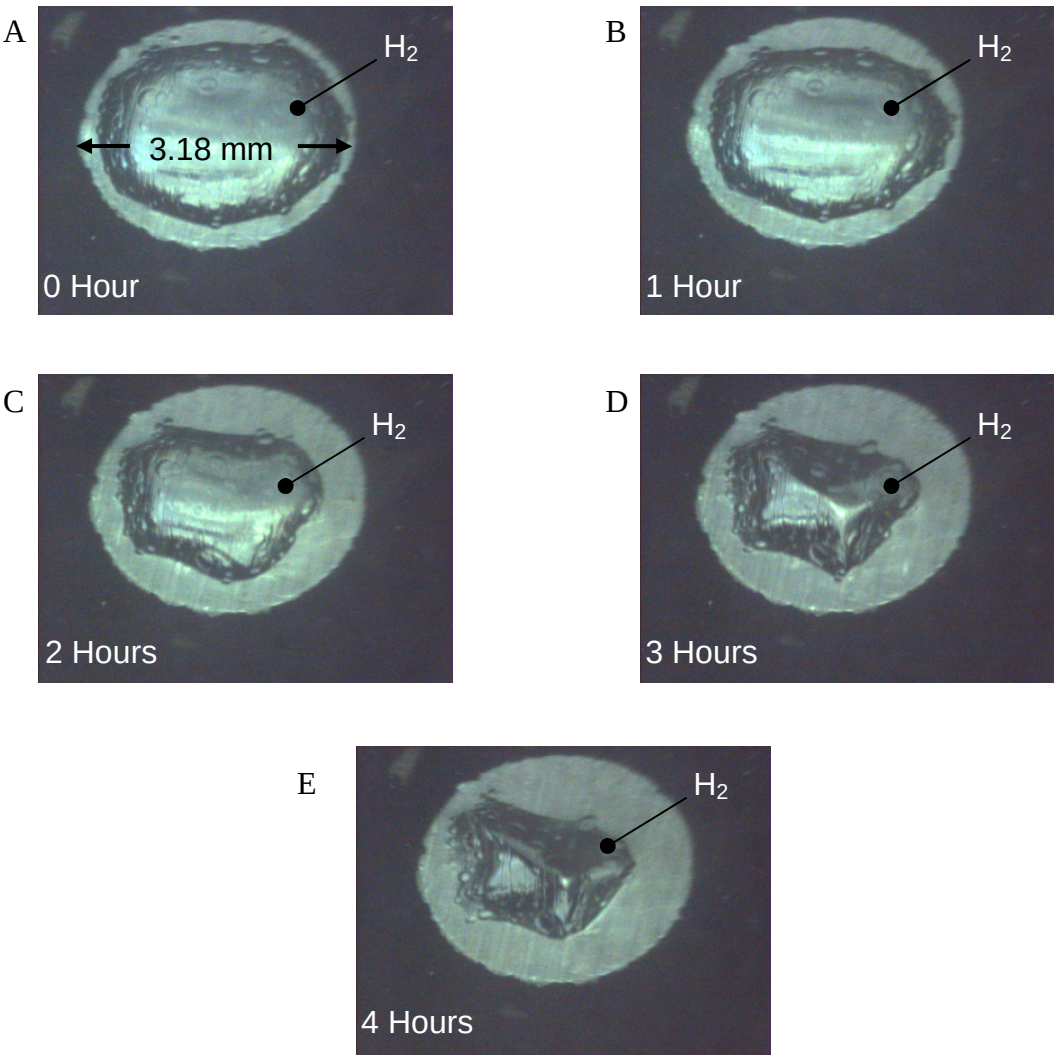

Figure 3.4 – Top view photographs of hydrogen bubbles on the cathode surface taken over a period of 4 hours.

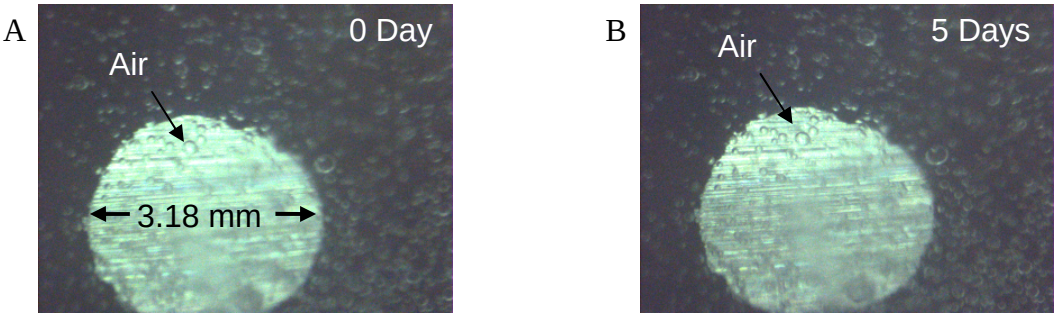

Figure 3.5 – Top view photographs of air bubbles in the bulk solution taken over a period of 5 days.

As can be seen in Figure 3.3 the oxygen bubbles, which appears as a film from the perspective, slowly fade away and only a small portion is visible after a period of 4 days. Alternatively, the hydrogen bubble in Figure 3.4, which is more discernable due to the shadowing along the edges, rapidly decreases in volume over a period of 4 hours. Although not shown, the oxygen bubble is not visibly present after a day. In Figure 3.5 there appears to be no change in the size of quantity of the bubbles after 5 days.

The enhanced black and white micrographs of the bubble on the electrode surface at pressures of 0 to 300 mmHg taken at 20 mmHg intervals are shown Figure 3.6.

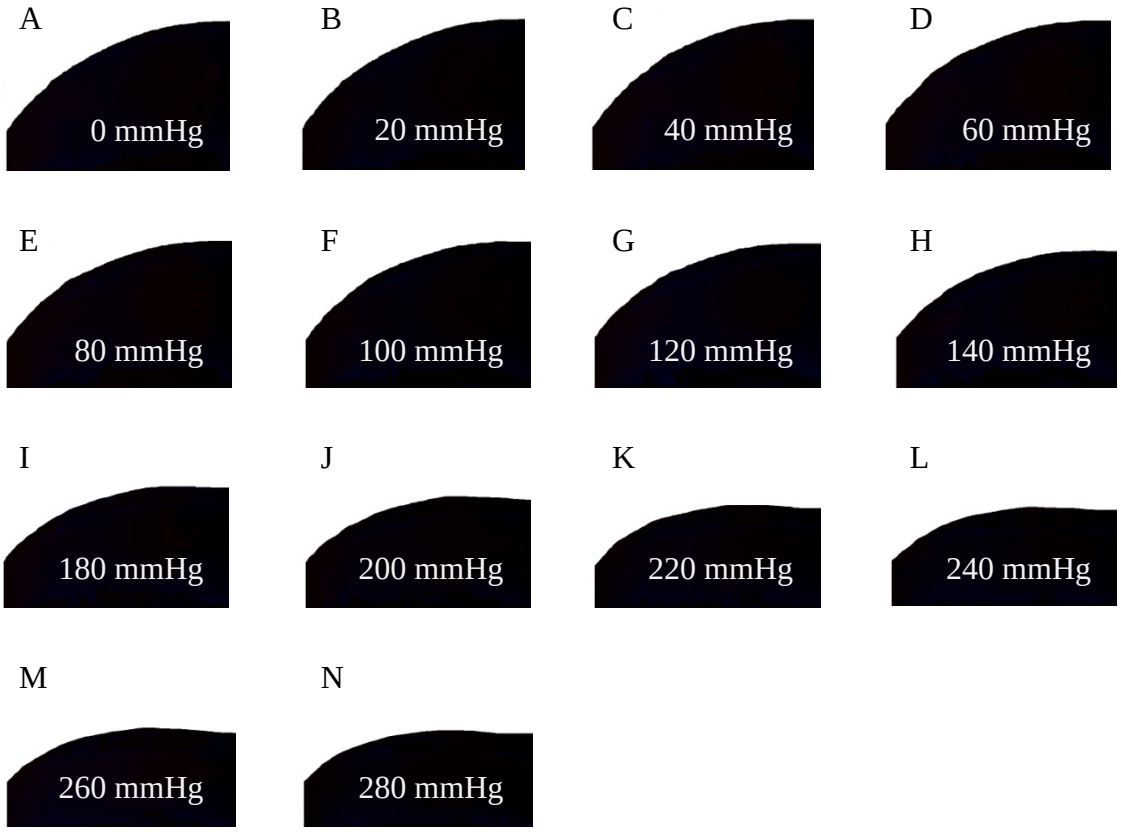

Figure 3.6 – Front view enhanced black and white micrographs of a bubble on top of an anode in an ECC, all images were taken at 25 ^{o}C. Images A – N were taken at increasing pressurization from 0 to 280 mmHg at 20 mmHg increments. Note: an image was not taken at 160 mmHg.

In Figure 3.6 from 0 to 120 mmHg there appears to be no visually perceivable change in the shape of the bubble, whereas, from 120 to 220 mmHg there is noticeable compression of the bubble. From 220 to 400 mmHg the bubble again appears to exhibit little visual change in the shape, specifically characterized by an inflection point near the right (axial) edge. Figure 3.7 is a plot of the change in volume due to pressurization, while Figure 3.8 is a plot of the change in surface area as a function of pressurization. The change in the real component of the impedance for the same sample that was used in the image analysis is plotted in Figure 3.9 for the same pressure range of 0 to 300 mmHg.

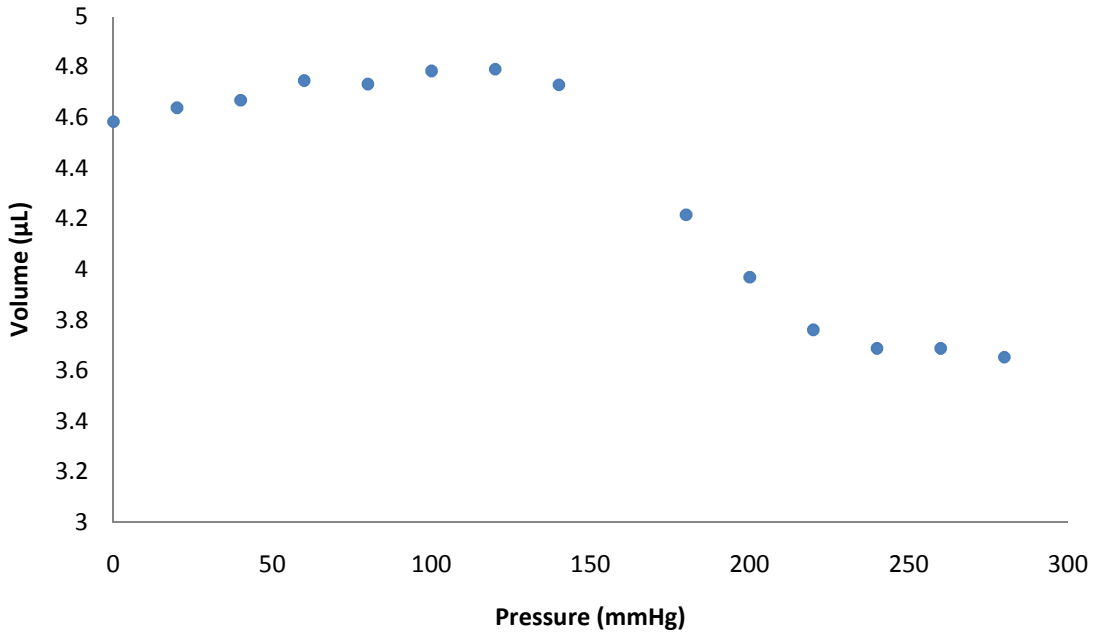

Figure 3.7 – Plot of the change in volume versus the change in applied pressure in an ECC with 17.5% gelatin, two aluminum electrodes, at 25 ^{o}C. The x-axis at the bottom of the plot has a range of 0 mmHg to 300 mmHg. The y-axis on the right-hand side of the plot has a range of 3 µL to 5 µL. Each solid blue circle represents the raw data.

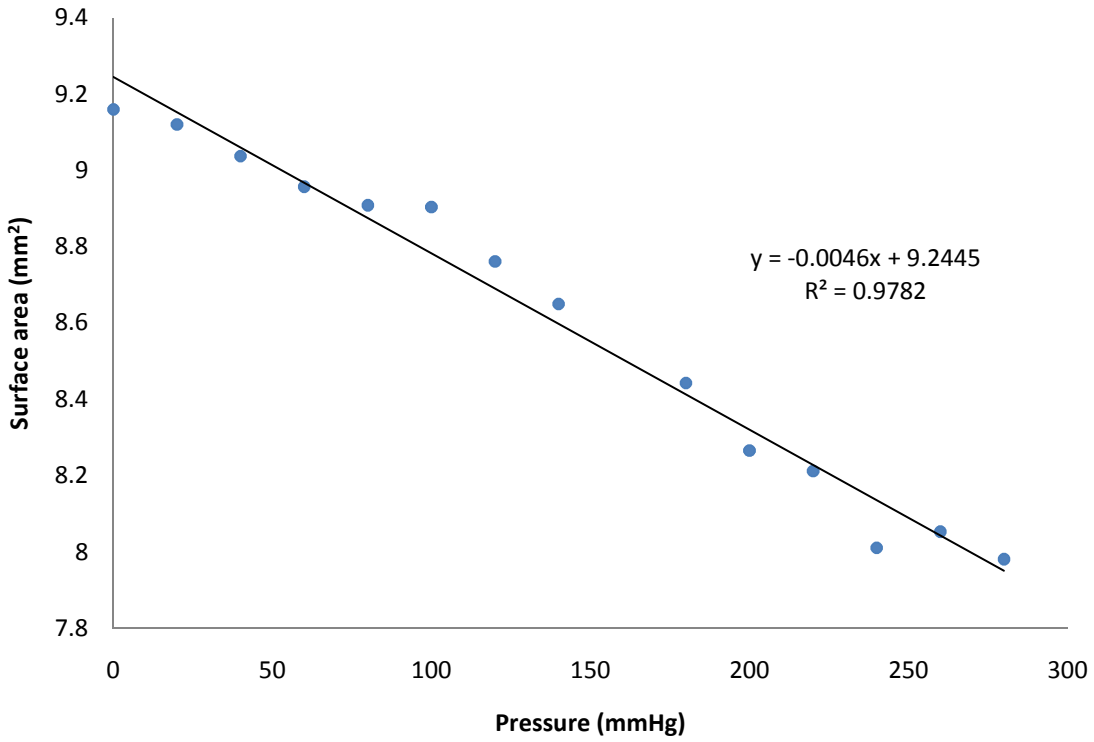

Figure 3.8 – Plot of the change in surface area versus the change in applied pressure in an ECC with 17.5% gelatin, two aluminum electrodes, at 25 ^{o}C. The x-axis at the bottom of the plot has a range of 0 to 300 mmHg. The y-axis on the left-hand side of the plot has a range of 7.8 mm^2 to 9.4 mm^2. Each solid blue circle represents the raw data. A least squared linear regression line is plotted through the data and is the reported on the plot along with the coefficient of determination denoted R^2.

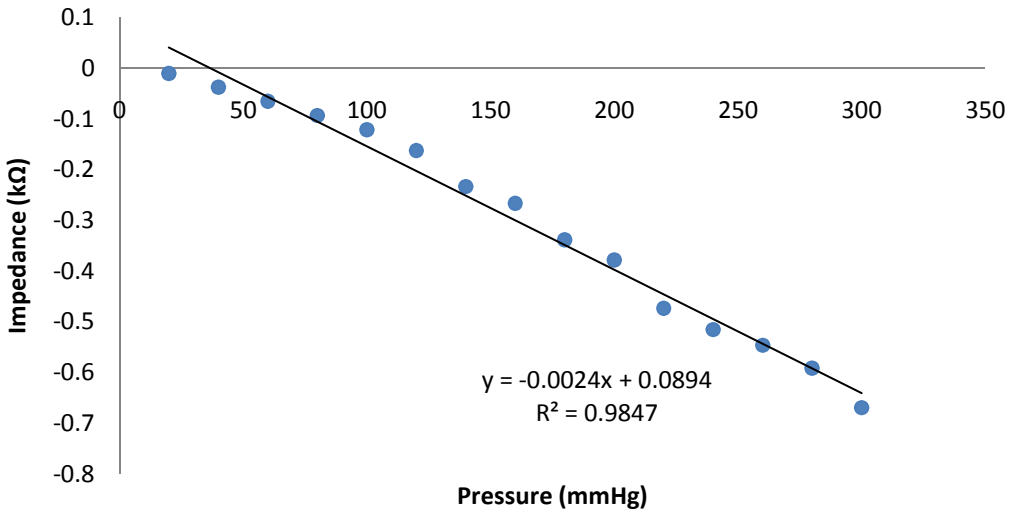

Figure 3.9 – Plot of the change in impedance versus the change in applied pressure in an ECC with 17.5% gelatin, two aluminum electrodes, at 25 ^{o}C. The x-axis at the bottom of the plot has a range of 0 to 300 mmHg. The y-axis on the left-hand side of the plot has a range of 0 to 800 ohms. Each solid blue circle represents the raw data. A least squared linear regression line is plotted through the data and is the reported on the plot along with the coefficient of determination denoted R^2.

3.5 Discussion

The bubble stability test was conducted to understand both how the stability of bubbles formed by electrolysis differ from those formed from cavitation as well as to determine which gas bubble would most likely only be affected by pressure (not time) thereby be best suited for imaging surface and volume behavior as a function of ambient pressure. While the images of the air bubbles (Figure 3.2 K and L) show that that it does not decompose over a period of five days, thus more suitable for stable sensor design, the images of bubbles on the electrode are compromised (distorted) by bubbles and are distributed in the bulk solution. The errors associated with bulk bubble formation deemed it necessary to use bubble formed by electrolysis at the electrode surface for all the mechanical deformation studies.

The question becomes, are the bubbles formed by cavitation similar to the bubbles formed during electrolysis? Both of these dispersed gas systems are formed after the majority of the crosslinked network is formed. Both form on the same nucleation sites either in the bulk material or at the electrode surface. At the electrode it will be the surface imperfections or roughness that are the site of nucleation where as in the bulk it will be regions on the amphiphilic macromolecule [51]. The observation that the air bubbles are stable and the oxygen and hydrogen bubble redissolve has little to do with the bubble physical geometry or structure and everything to do with the need to obtain a chemical equilibrium. Two potential reasons for the decay of the oxygen and hydrogen bubbles are: (1) The partial pressure of oxygen and hydrogen in the solution is around 21% and 0% (e.g., that of air), yet the bubble is either 100% oxygen or hydrogen. The resulting concentration gradient will drive both oxygen and hydrogen to dissolve back into the solution. This is also supported by the Figure 3.2 A-J; since there is a larger partial pressure gradient between the hydrogen gas and dissolved hydrogen in solution than the oxygen gas and dissolved oxygen in solution, it would be expected that the rate of diffusion would occur more quickly for the hydrogen gas. (2) As the open circuit voltage in the ECC drops below 1.6 Volts, the dissolved hydrogen in the bulk solution in contact with the oxygen at the anode will combine to generate water. Likewise, the dissolved oxygen will combine with the hydrogen gas at the cathode. We are therefore, confident that the physical and geometric characteristics of electrolyzed bubbles are the same as cavitation bubbles.

Due to the longer stability of the oxygen gas and the preferential locality to the electrode surface, it was selected for the mechanical deformation study. The

pressurization study was conducted immediately after electrolysis. During electrolysis a large bubble was created to span the entire electrode surface to facilitate both the imaging and image analysis, but also to determine if the ECM response resulted from a change in the surface area of the electrode/bulk solution interface or a change in surface area of the bubble/bulk solution interface.

Even though in this experiment the bubble completely covered the entire electrode surface eliminating any possibility for the electrode to contact the bulk solution, electric charge was able to conduct through the ECC. In fact the response in Figure 3.9 is linear like the response observed in chapter 2 (Figure 2.10). Gasses are extremely poor electrical conductors, therefore the only way charge transfer could occur is if the bubble was actually an aerogel containing solid, conductive gelatin network.

From the plot of volume versus pressurization in Figure 3.7; it shows that the volume increases from 0 to 120 mmHg at a constant rate. This could be due to water vapor or other dissolved gaseous nearby being forced into the bubble. From 120 to 220 mmHg, the volume decreases at a sharp rate which is visible in Figure 3.6 G-K. From 220 to 280 mmHg, the volume continues to decrease but at a shallower slope, which is also visible in Figure 3.6 K-N. The fact that the volume versus pressure curve is not linear for the range of 0 to 280 mmHg eliminates the possibility that a volume or density effect is driving the change in ECM response.

Finally, the surface area versus pressurization plot in Figure 3.8 and the change in impedance versus pressure in Figure 3.9 provides the definitive evidence in support of the hypothesis that the surface area is linearly related to pressure for the range of 0 to 280

mmHg and that the ECM response is due to a change in surface area of the aerogel electrode.

3.6 Conclusions

Two conclusions can be draw from this effort. First, the electrolysis in a gelatin hydrogel generates an aerogel rather than single phase gas bubbles. Second, the change in surface area of the aerogel in contact with the bulk solution is linearly related to the applied pressure. These findings are necessary to support the overall hypothesis that the ECM response to pressure is due to a change in the surface area of the aerogel electrodes. The response was found to be linear for the range of 0 to 280 mmHg, which is in the useful range for medical device applications [52]. Moreover, we have demonstrated that the area change is linear regardless of the bubble size thus the total change in area from a distribution of bubble sizes or a single large bubble remains linear with changes in pressure yielding a linear voltage response. This is ideal for manufacturing where tight control over bubble size and distribution would be difficult to control and/or measure. However, further studies will need to be conducted to determine the feasibility of using an ECC for pressure measurement in the gastro intestinal tract.

4 Efficacy of an Electrochemomechanical Pressure Transducer for use in the Gastrointestinal Tract

4.1 Introduction

Dysphagia is the medical term used to describe the sensation in the difficulty of swallowing [52]. This symptom has a high incidence in the elderly with a reported 7-10% of adults over 50 seeking medical attention [53,54]. Additionally 25% of all hospitalized patients experience swallowing disorders [55]. The diseases that cause dysphagia are generally categorized into two stage of deglutition (the act or swallowing), oropharyngeal and esophageal.

The oropharyngeal stage of deglutition begins with the coordinated efforts of the tongue and the muscles of mastication to chew, mix food and saliva together, and push the bolus into the oropharynyx, where the involuntary swallowing reflex is triggered by the cerebellum. The soft palate elevates to close the nasopharynx, and the muscles pull the larynx up and forward. The epiglottis moves downward to cover the airway while striated pharyngeal muscles contract to move the food bolus past the upper esophageal sphincter (UES) and into the proximal esophagus [56]. See Figure 4.1 for anatomical diagram of swallowing process.

The causes of orapharyngeal swallowing disorders are numerous and include neuromuscular disease such as cerebrovacular accidents, multiple sclerosis, Parkinson's disease, brainstem tumors, pseudobulbar palsy, peripheral neuropathy, and muscular diseases (myasthenia gravis, poliomyelitis, dermatomyositis). Orapharyngeal swallowing

disorders are also caused by mechanical obstructions such as thyromegaly, cervical lymphadenopathy, oropharyngeal carcinomas, congetical abnormalities, inflammatory disorders, and hyperstosis of the cervical spine [52].

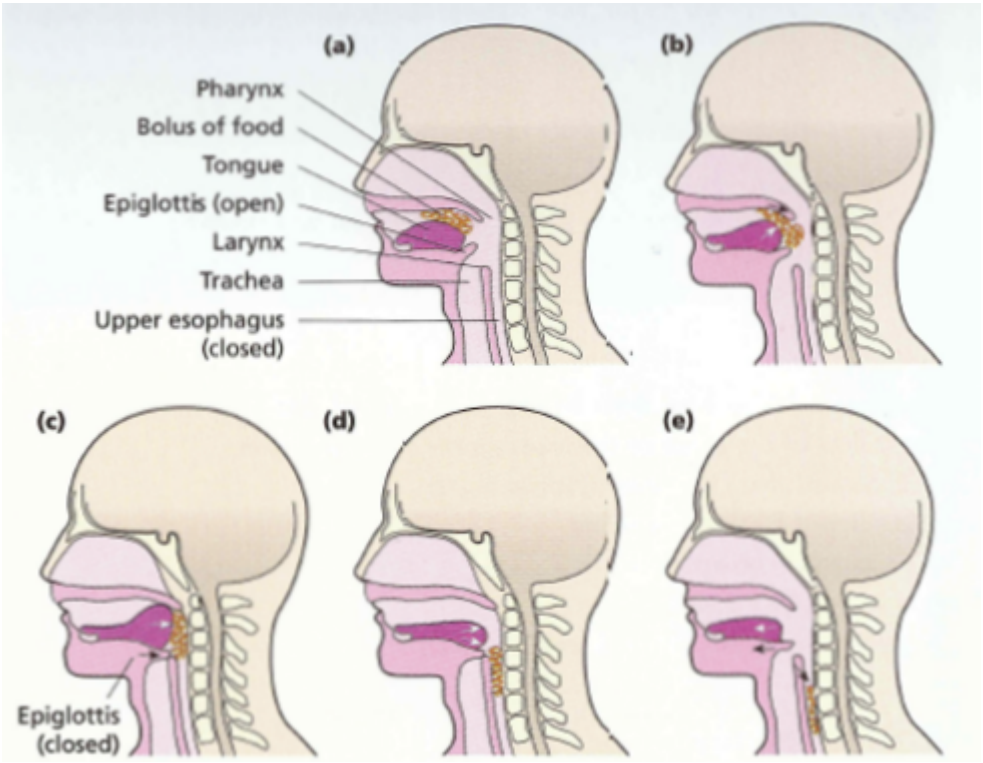

Figure 4.1 – Anatomical diagram of the swallowing process [52].

The esophageal stage of deglutition begins as food is propelled from the pharynx into the esophagus. The medulla oblongata initiates involuntary contractions of the skeletal muscles of the upper esophagus to force the bolus through the mid and distal esophagus. The lower esophageal sphincter (LES) relaxes and the food bolus is propelled into the stomach [56].

The causes of orapharyngeal swallowing disorders have not been completely defined but include the absence of inhibitory neurotransmitters, degeneratice changes in

the vagus nerve, erosive esophatigitis, stricture, Barrett's esophagus, and aspiration pneumonia [52].

The many causes of dysphagia have led to the differential diagnosis of the upper GI tract which includes the following conditions: Achalasia, which is the condition characterized by inability of the LES to completely relax, preventing the passage of food into the stomach [57]. Zenker's diverticulum, which is a hernia located at the border of the pharynx and the esophagus [58]. Gastroesophageal reflux disease (GERD), which is the retrograde movement of gastric content through the LES into the esophagus [59]. Scleroderma, which is the fibrosis or hardening of internal organs [60]. Neoplasia, which is the abnormal growth of tissue including both benign and malignant cells [61].

Endoscopy is a procedure that allows practitioners the ability to look inside the hollow organ to visualize obstruction in the esophagus and identify inflammation or neoplasm of the tissue. This technique can provide information at a specific site, but fails to capture information of the interactions of the entire system or organs. Videoradiography is the technique of taking sequential x-ray frames of an individual swallowing a barium bolus. This allows practitioners the ability to study the kinematics involved during a swallow. Missing from both of these procedures is the pressure or force information along the esophagus. This information is useful for when imaging procedures are inconclusive, particularly when the pathology is characterized by elevated pressures. Intra esophageal pressure measurement, also called manometry is a minimally invasive diagnostic procedure used to investigate pressure profiles in the upper GI tract.

Manometry recordings correlates spatial, temporal and pressure measurements during a procedure. It defines the dimensions of the organs under study by sweeping a

pressure sensor through the upper GI tract and correlating the pressures to known physiological ranges. The location and lengths of the LES, esophagus, and UES may be determined, along with the location of the stomach. Swallowing contractions or peristalsis can be monitored by having an array of pressure sensors along the esophagus. In addition to peristalsis, the relaxation and closure of the UES and LES can be investigated. GI abnormalities can be identified by regions of abnormal pressure, incomplete or biphasic peristalsis, and prolonged or shortened contractions in the esophagus.

The characteristics of each disease are a little different in needs and methods as such we will review the ranges to provide a complete landscape for pressure sensing needs/specifications. For symptoms such as nutcracker esophagus, pressures may exceed 300 mmHg; therefore it is important for the pressure sensors to be able to measure this. For many manometric procedures a baseline pressure is calculated by averaging the pressure along the esophagus. The analysis of the studies compared measured pressures to the baseline pressure, which means it is critical that there is little or no drift in the sensing element, but that the absolute pressure is not required instead only the relative pressure difference. Also, it is normal for physiological pressures in the UES and LES to drift, so this drift must be distinguishable from sensor drift.

For non-manometeric studies of the esophagus, such as GERD, pressure sensing is used to position the pH and impedance sensors located in a catheter properly above the LES for 24 hour measurement. The stomach rests beneath the diaphragm while the esophagus sits in the thoracic cavity. During breathing the esophagus experiences a decrease in pressure with each inspiration on the order of 2-5 mmHg, while the stomach

will experience an increase in pressure of roughly the same magnitude. The pressure sensor must be sensitive enough to measure these small signals for the placement of the catheter.

GERD studies will take pressure measurements at the beginning of the procedure until the catheter is properly placed, while manometry procedures can take up to an hour to perform. Cough studies can take up to 24 hours to perform. This involves combining a GERD study with pressure measurement in both the esophagus and stomach. The premise being that cough can be detected as a high pressure spike that occurs in each zone simultaneously. In cough studies, the identification of the cough temporal position relative to a reflux episode is important and not the actual pressure of the recorded cough.

The current technology used to perform manometry can be classified as either solid state pressure sensors or fluid infused catheters. Solid state pressure measurement includes piezoresistive and capacitive based sensors located in the catheter itself. These sensors are considered accurate and easy to calibrate. These sensor have many drawbacks, they are expensive, require sterilization for reuse, and typically unidirectional although the trend is moving towards omni-directional sensors. Fluid infused catheters require a separate lumen for each pressure channel, in which the pressure is transmitted through a column of fluid to an external pressure sensor. These sensors also have many drawbacks, for example there is a physical limit to the number of lumens that can physically fit in the catheter and the entire column of fluid is subject to pressure, not just the opening of the channel.

The use of an EPT will be evaluated performance under GI pressure measurement conditions and develop techniques to overcome specific issues that could hinder proper

diagnosis. The studies conducted in Chapters 2 and 3 have shown drift in an ECC due to pressurization. Thus one focus of the current investigation is to develop techniques to reduce, mitigate, or eliminate the drift in an ECC. We will also explore the dynamic range of the EPT to ensure suitability for the entire range of GI investigations.

4.2 Materials

Type A gelatin from porcine skin with 175 bloom strength and 37% formaldehyde in water were obtained from Sigma-Aldrich (St. Louis, MO).

6061 Aluminum rods, 26-gauge copper magnet wire, and Loctite® 401 cyanoacrylate adhesive were obtained from McMaster-Carr (Elmhurst, IL).

Simulated gastric fluid standardized for 0.2 NaCl (w/v) and 0.7 HCl (v/v) was obtained from Cole-Parmer (Vernon Hills, IL).

4.3 Methods

Preparation of Gelatin Hydrogels

Gelatin hydrogel (gel) samples were prepared at 17.5% concentrations by weight in deionized water and were 100% crosslinked based on the theoretical number of crosslinking sites on each gelatin molecule. The gel was heated up to 70 ^{o}C while being constantly stirred by a magnetic stirrer until the gelatin was fully dissolved. The gel was exposed to a vacuum which was constantly adjusted to prevent boil over for a period of ten minutes. Formaldehyde was then added and the gel was continually stirred at a slower rate. The gel was then poured into its desired container and a vacuum was then applied for ten minutes, again constantly adjusted to prevent boil over. The vacuum was

then removed and the gel was allowed to cool to its test temperature. The gel then remained at this temperature for a period of 24 hours.

Current Measurement

The constant voltage test was performed to determine how applying a fixed voltage would affect the ECM response. By applying a constant voltage, either the impedance or the current could be measured. The current was selected to be measured due to the setup of the potentiostat. If an equal but opposite voltage to the OCV is applied, there will be 0 resultant current flowing through the system. If the sum of the applied voltage and OCV is greater than 1.23 Volts, then the electrolysis of water will occur [16]. Since electrolysis is unwanted for this test, and the goal is to see a measurable change in the current through the ECC, a minimum and maximum value for the applied voltage was determined. The measured OCV of the ECC was at -110 mV, this meant that the applied voltage would be bound between -1.12 V and 1.34 V, excluding 110 mV. The applied voltage was selected to be -250 mV giving a net polarity across the ECC of 360 mV. An ECC with two aluminum electrodes was electrolyzed 24 hours prior to testing to stabilize the OCV. The OCV was measured and a DC voltage was applied. The current was measured as 517 mmHg square waves were applied.

Impedance Measurement

When measuring the change OCV or current to pressure, there has always been an observed drift in current or voltage immediately following the pressurization. This is due to the ECC reestablishing a new equilibrium to the newly change in voltage of the cell.

The idea behind applying an AC signal and measuring the impedance is that the signal can be applied with respect to the ever changing OCV. Also since the applied signal is a sine wave, any polarization due to the positive crest of the wave will theoretically be canceled out by the negative trough. The purpose of the impedance test is to investigate the effect of frequency on the response, drift, and noise in the sample. From the EIS data in Figure 2.8, it can be seen that the impedance changes across the entire bandwidth, however it does not provide any information on the drift or noise at each frequency. An ECC with two aluminum electrodes was electrolyzed 24 hours prior to testing to stabilize the OCV. A 10 mV AC signal was applied to the test sample repeatedly with frequencies of 10 Hz, 50 Hz, 100 Hz, 500 Hz, 1 kHz, 5 kHz, 10 kHz, 50 kHz, and 100 kHz for 90 seconds at each frequency. From a period of 30 – 60 seconds a 517 mmHg pressure was applied to the samples. The total impedance and the real component of the impedance were recorded.

A second test in which the impedance of the sample was measured at a frequency of 500 Hz was conducted. The gel was exposed to a pressure which was ramped up from 0 to 3100 mmHg. At each 517 mmHg interval the pressure was held constant for 10 seconds.

Gastric Simulation

The purpose of the gastric simulation test was to emulate the effects of having a sensor in both the esophagus and the stomach for a period of 24 hours. Two EPT were created by filling 0.5 inch pieces of Teflon™ tubing containing two copper magnet wires. The enamel on the ends of the magnet wires were stripped back $1/10^{th}$ inch to expose the

copper to the gel. The exposed ends of the wires were spaced 1/5th inch tip to tip see Figure 4.2.

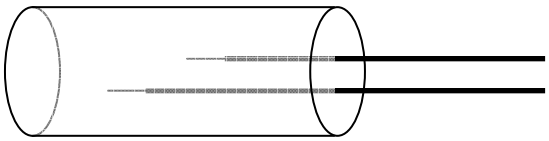

Figure 4.2 – Illustration of EPT

After the gel cured the EPTs were inserted into a glass cell with one sensor at the bottom surface (i.e., in stomach sensor) and the other sensor suspended 1 inch above the bottom surface (i.e., in esophagus sensor). After the EPTs were positioned inside the glass cell, the EPTs were then electrolyzed. Simulated gastric fluid warmed to 37 ^{o}C was then added to the glass cell in sufficient quantity to submerse the EPT at the bottom of the cell, but not enough to make contact with the suspended EPT. The electrodes inside the EPTs were located ¼ inch from the surface, surround by either a solution containing NaCl and HCl or air. The glass cell was pressurized to 517 mmHg periodically over a period of 24 hours while maintaining a temperature of 37 ^{o}C, starting immediately after contact with the simulated gastric fluid. The impedance of the EPTs was recorded while a 10 mV, 500 Hz AC signal was applied during the pressurization cycles.

4.4 Results

The constant voltage test was conducted to determine the effect of drift as a constant voltage is applied. The external voltage was applied at 250 mV and the ECC was pressurized to 517 mmHg, held at this pressure for approximately 10 or 20 seconds and then the pressure was removed. The pressure impulse was cycled for a total of 4

times. Figure 4.3 shows the results of this test. On the third cycle of the pressurization a slight ripple can be seen, this is due to an accidental drop and restoration of the pressure.

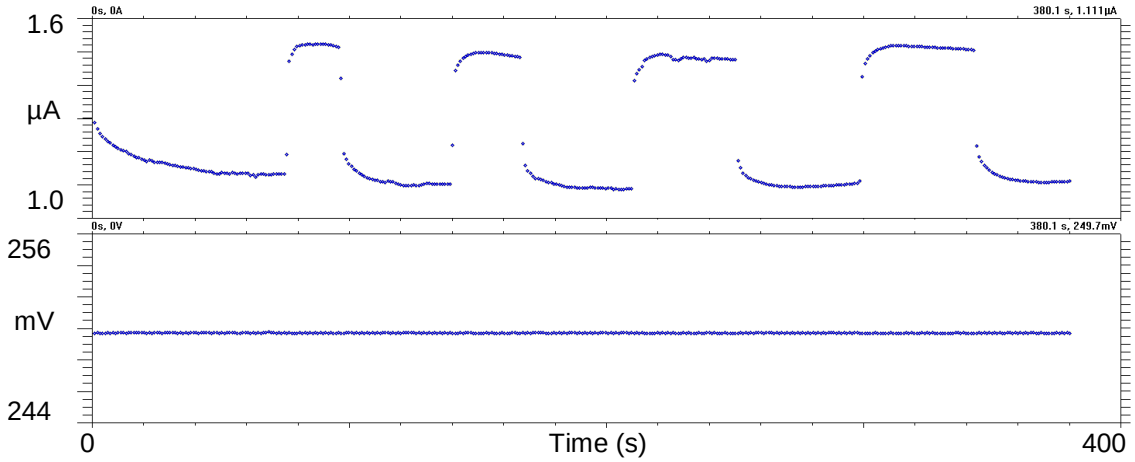

Figure 4.3 – Plot of current versus time with an applied potential of 250 mV. The ECC was pressurized 4 times at 517 mmHg at 10 and 20 second intervals.

The raw data from the 100 and 500 Hz is shown in Figures 4.4 as plots containing both the total impedance and the real component of the impedance. The response for the total and real component of the impedance are summarized in Figure 4.5 for each frequency in which the response is calculated from Equation 4.1, where $Z_{real\ (0\ mmHg)}$ is the measured real component of the impedance immediately before pressurization and $Z_{real\ (517\ mmHg)}$ is the measured real component of the impedance immediately after pressurization. The drift for the total and real component of the impedance are summarized in Figure 4.6 for each frequency in which the drift is calculated from Equation 4.2, where $Z_{real\ (30\ sec)}$ is the measured real component of the impedance immediately after pressurization, and $Z_{real\ (60\ sec)}$ is the measured real component of the

impedance immediately prior to removing the applied pressure. The signal to noise ratio (SNR) for the total and real component of the impedance are summarized in Figure 4.7 for each frequency in which the SNR is calculated from Equation 4.3, where the Z_{real} rms noise is based on the noise from a least squared regression fit of the drift.

$$Response = \frac{Z_{real(0\ mmHg)} - Z_{real\ (517\ mmhg)}}{Z_{real\ (0\ mmhg)}} \cdot 100\% \quad 4.1$$

$$Drift = \frac{Z_{real\ (30\ sec)} - Z_{real\ (60\ sec)}}{Z_{real\ (30\ sec)}} \cdot 100\% \quad 4.2$$

$$SNR = 20 \cdot \log\left(\frac{Z_{real(0\ mmhg)} - Z_{real\ (517\ mmHg)}}{Z_{real}\ rms\ noise}\right) \quad 4.3$$

A

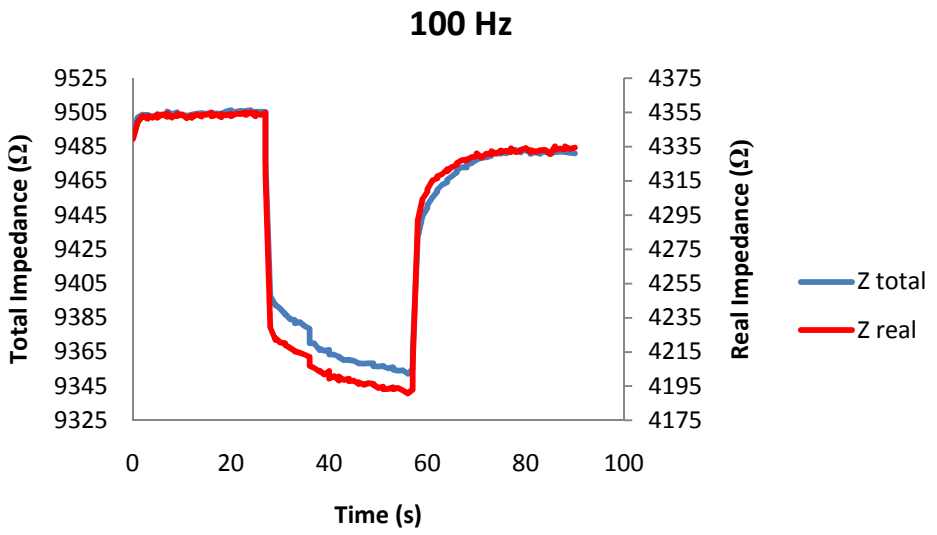

B

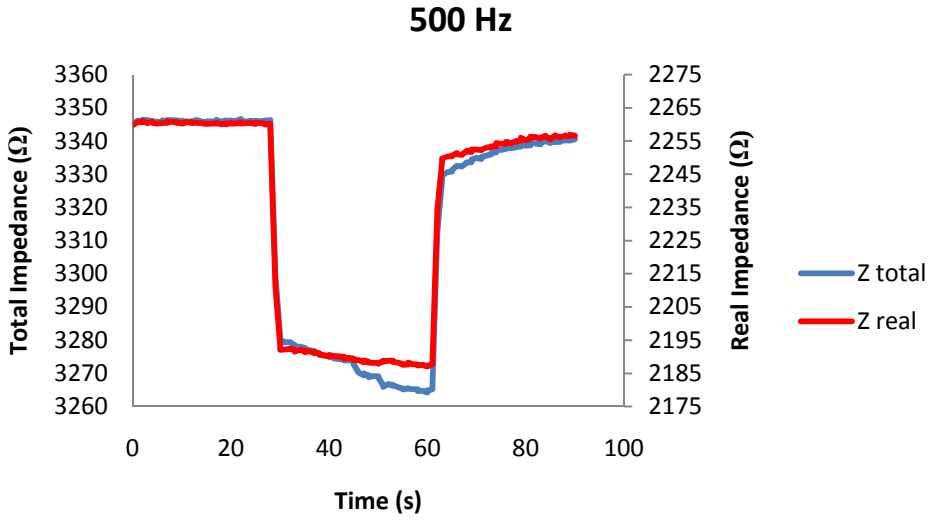

Figure 4.4 – Plots of impedance versus time. Plot A refers to a 100 Hz test signal, while plot B refers to a 500 Hz test signal. In each plot the blue and red lines are the measured total and real components of the impedance respectively. The left axis is in ohms and corresponds to the total impedance; the right is also in ohms and corresponds to the real component of impedance. In each plot the ECC was pressurized to 517 mmHg during the time frame between 30 and 60 seconds.

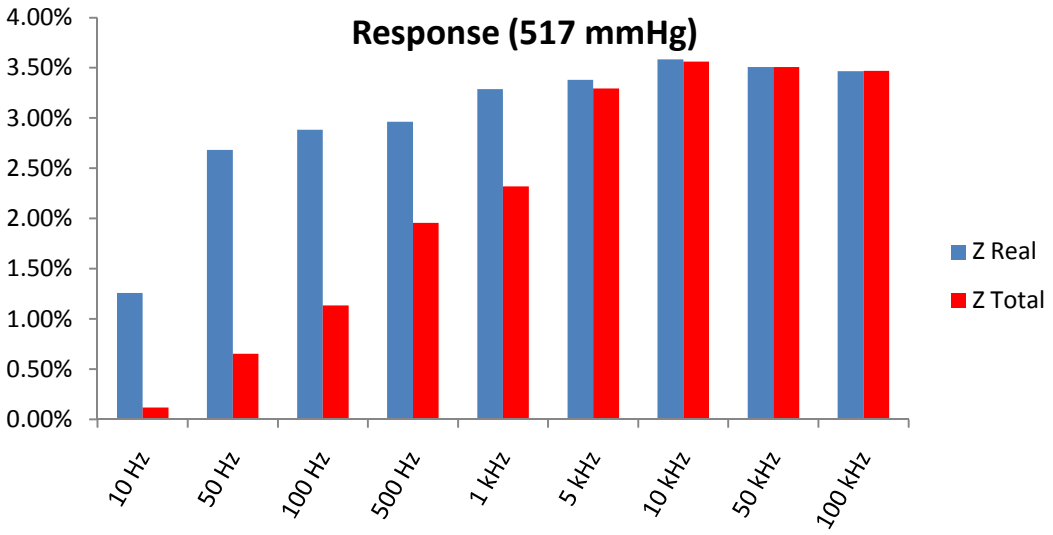

Figure 4.5 – Bar graph of the percent change in impedance due to a 517 mmHg pressure impulse. The blue bars represent the real component of the impedance, while the red bars represent the total impedance. Each set of bars are graphed next to their associated frequency.

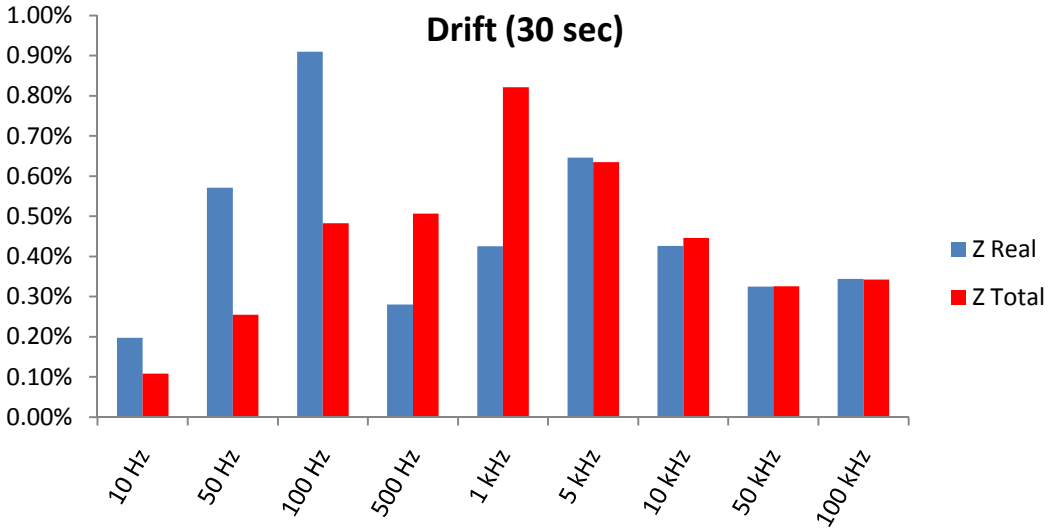

Figure 4.6 – Bar graph of the percent change in drift due to a 517 mmHg pressure impulse. The blue bars represent the real component of the impedance, while the red bars represent the total impedance. Each set of bars are graphed next to their associated frequency.

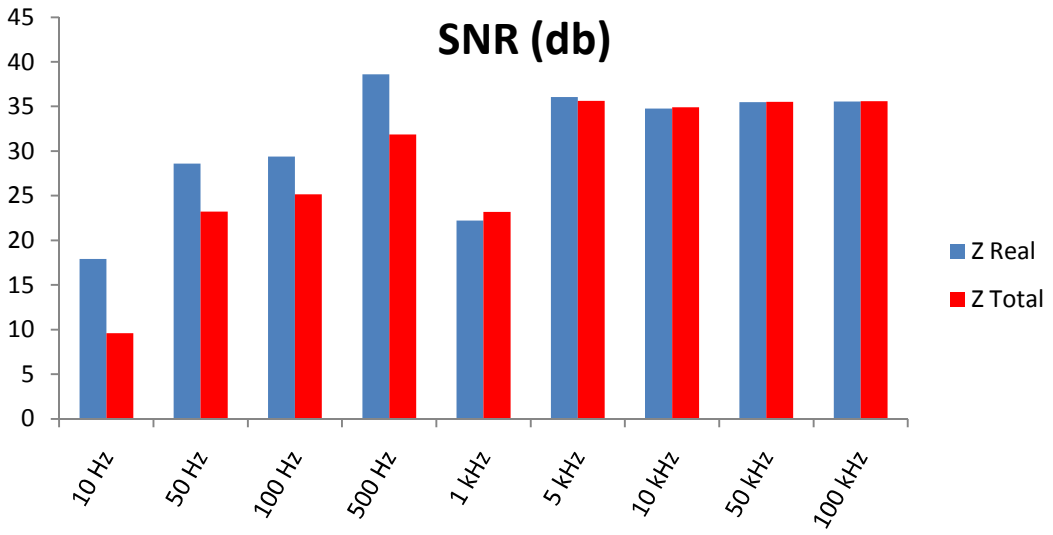

Figure 4.7 – Bar graph of the signal to noise ratio of the drift for each frequency. The blue bars represent the real component of the impedance, while the red bars represent the total impedance. The SNR is reported in decibels.

A pressure range test was conducted to investigate the behavior of the gel at a pressure range of 0 to 3100 mmHg. The pressure in the gel was ramped up at 517 mmHg intervals, at which point it was held constant for 10 seconds. During the range of 2586 to 3100 mmHg the glass cell containing the gel shattered due to the high pressure, resulting in the pressure returning back to atmospheric pressure. The impedance was measured while a 10 mV, 500 Hz signal was applied to the gel. The raw data from the test is shown in Table 4.1.

Table 4.1 – Pressure and impedance of ECC for pressure range test. The impedance was measured 10 seconds after the pressure was obtained. The glass cell shattered between pressures of 2586 and 3100 and the impedance was measured after the pressure returned to atmospheric.

Pressure (mmHg)	*Impedance (Ω)*
0	2325
517	2318
1034	2311
1550	2307
2070	7.91E+05
2586	6.90E+07
0	5.40E+07

The impedance was measure periodically before and during a 517 mmHg pressure was applied to the EPTs. Figure 4.8 plots the 0 mmHg impedance as a function of time during the test while Figure 4.9 plots the pressure response defined by Equation 4.1, also as a function of time. Figures 4.10 and 4.11 show the pressurization cycle taken at 4 hours into the test for both the gastric and air response to the pressurization.

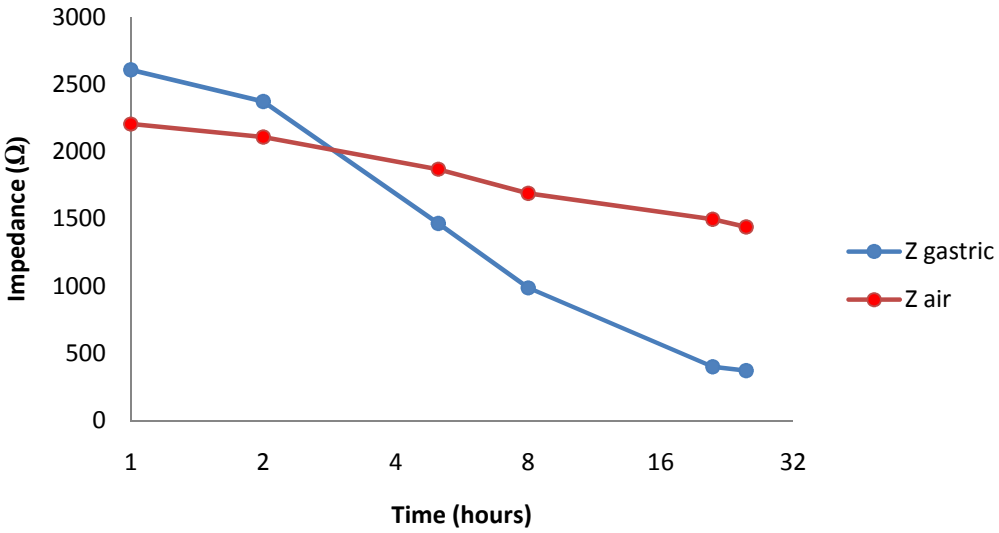

Figure 4.8 – Plot of total impedance versus time, the gastric impedance was measured from an EPT submersed in simulated gastric fluid, while the air impedance was measured from an EPT suspended above and not touching the simulated gastric fluid. Time is plotted on a log (base 2) scale.

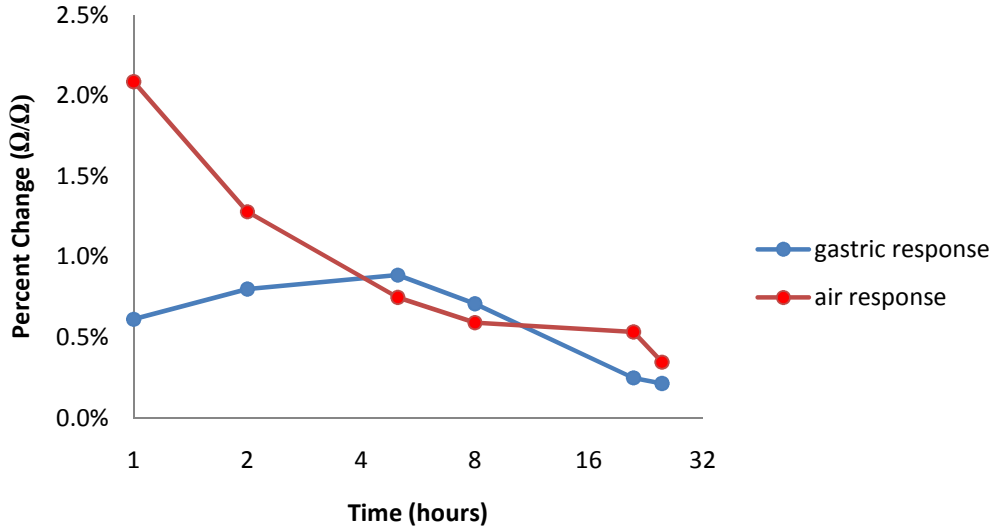

Figure 4.9 – Plot of change in impedance versus time, the gastric impedance was measured from an EPT submersed in simulated gastric fluid, while the air impedance was measured from an EPT suspended above and not touching the simulated gastric fluid. Time is plotted on a log (base 2) scale.

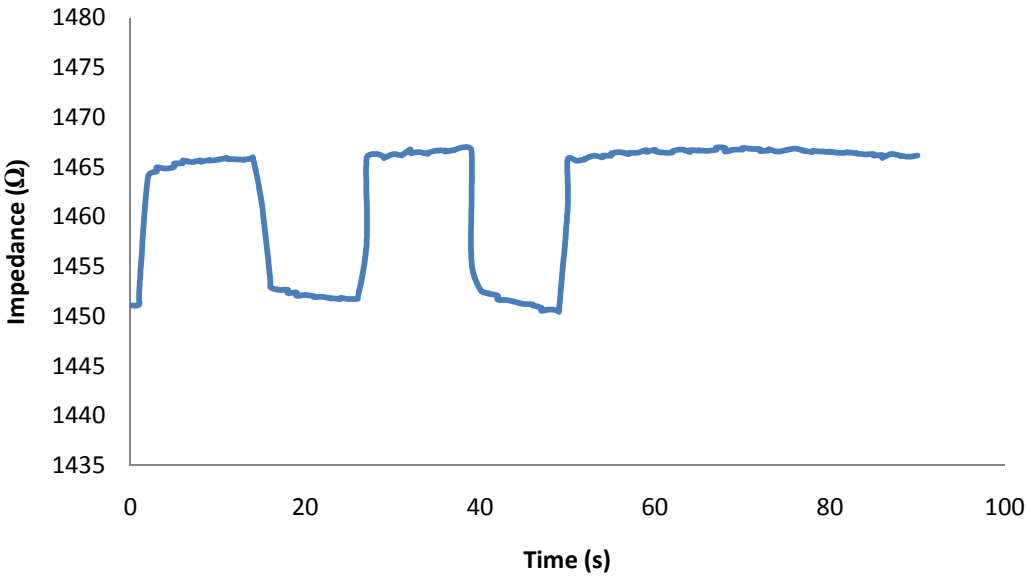

Figure 4.10 – Plot of impedance versus time, the impedance was measured from an EPT that was submersed in simulated gastric fluid while the glass cell was pressurized three times to 517 mmHg.

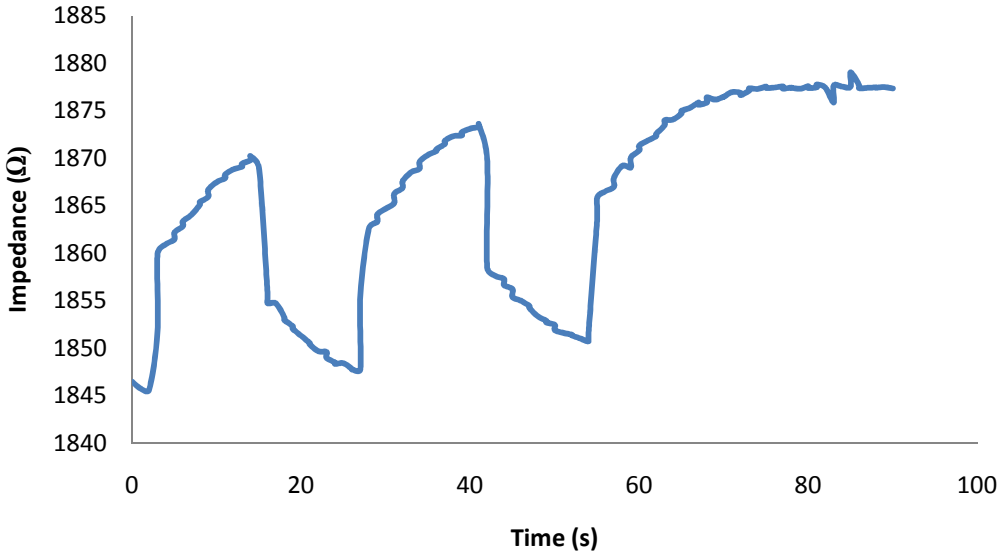

Figure 4.11 – Plot of impedance versus time, the gastric impedance was measured from an EPT that was suspended above simulated gastric fluid while the glass cell was pressurized three times to 517 mmHg.

4.5 Discussion

From visual inspection of the data in can be seen that there is a slight drift between each of the pressurizations, and that this drift continues as a function of time whether the pressure is held high (517 mmHg) or low (0 mmHg). The baseline current also varies with pressurization starting at 1.14 µA and varying to a low of 1.10 µA. Regardless of the initial current, the magnitude of the change in current due to a 517 mmHg pressure increase or decrease was always 0.40 µA. The baseline drift was 10% of the response, which is significant improvement over measuring the OCV response; from Chapter 2 the baseline drift as large as 50% of the response.

The frequency test was performed to look at the effects of pressure on both the total and real components of the impedance. The ideal response is to see a matching square wave output in impedance for the square wave input in pressure. By investigating just the real component of the impedance, any capacitive charging and discharging effects will be negated. Also the impedance profile of the real impedance resembles the applied square wave pressure more so than the total impedance at frequencies above 100 Hz, that is to say that the there is less drift following the applied pressure and less drift upon removing the pressure. The reason that is more evident in the real impedance is that the total impedance has capacitive components, and there is a stored charge that must be slowly dissipated as the OCV changes. The signal to noise ratio is larger for the real component of the impedance than the total impedance for all frequencies tested except for 1 kHz. The SNR improves as frequency increases up 500 Hz then it tends to level off at around 38 db with exception to the 1 kHz signal. This could be due to either electromagnetic interference or resonance in the sample. The mechanical resonance is

coupled to electrical resonance by the ECM response. If an AC signal is applied to the sample, the ECM response will cause mechanical oscillations at that frequency. If the applied signal is close to the mechanical resonant frequency of the system, the magnitude of the oscillation will increase and induce changes in voltage potential.

During all tests the temperature was held constant at 37^{o}C and the effect of temperature was not investigated. The temperature in the body is relatively stable for short periods of time; however, the temperature of a bolus during swallowing doesn't necessarily reach body temperature and can cause small changes in temperature. Equations 4.4 – 4.7 show the equivalent circuit elements of Randle's circuit for bulk resistance (R_{Bulk}), bulk capacitance (C_{Bulk}), capacitive double layer (C_{dl}) and charge transfer resistance (R_{ct}); where l is the spacing between electrodes, F is Faraday's constant, μ_g is the electric mobility, c_g is the concentration of charge carriers, A is the surface area of the electrodes, cf is fringe effects correction factor, ε_o is the permittivity of free space, ε_r is the dielectric constant, R is the universal gas constant, T is temperature, n is the number of electrons transferred in a half cell reaction, and I is exchange current. The equation for the electric mobility is derived from the diffusion coefficient (D_g); both Equations are given as 4.8 and 4.9 respectively, where q_g is the charge per molecule, k is Boltzmann's constant, η_g is viscosity, and d_g is the effective diameter of the charge carrier. The Nernst equation is given as Equation 4.10, where E is the voltage potential, E^o is the standard electrode potential, and c_j is the concentration of species ĵ.

$$R_{Bulk} = \frac{l}{F \cdot \mu_g \cdot c_g \cdot A \cdot cf} \quad 4.4$$

$$C_{Bulk} = \frac{\varepsilon_o \cdot \varepsilon_r \cdot A \cdot cf}{l} \quad 4.5$$

$$C_{dl} = \left(\frac{\varepsilon_o \cdot \varepsilon_r \cdot F^2 \cdot c_g}{R \cdot T}\right)^{\frac{1}{2}} \cdot A \cdot cf \quad 4.6$$

$$R_{ct} = \frac{R \cdot T \cdot A}{n \cdot F \cdot i} \quad 4.7$$

$$\mu_g = \frac{q_g \cdot D_g}{k \cdot T} \quad 4.8$$

$$D_g = \frac{k \cdot T}{3 \cdot \pi \cdot \eta_g \cdot d_g} \quad 4.9$$

$$E = E^0 + \frac{R \cdot T}{n \cdot F} \cdot \left(\sum_{ox} \ln c_j - \sum_{red} \ln c_j\right) \quad 4.10$$

It can be seen that temperature (T) is present in both R_{ct} and C_{dl}. Even though temperature (T) in the electric mobility (μ_g) cancels out in Equations 4.8 and 4.9; R_{Bulk} is a function of the viscosity η_g which is temperature dependant. If the electric potential of the ECC is held constant and the temperature changes, then the ratio of the natural log of the concentration must change from the Nernst equation. Both R_{Bulk} and C_{dl} are functions of the concentration of charge carriers and the ion exchange current (i) in R_{ct} is also a function of the concentration. Physiological swallow simulations with an encapsulated sensor will be needed to determine the effect of a change in temperature resulting from a bolus swallow; however, the effect can be reduced by eliminating the capacitive components out of the circuit. This is accomplished by investigating the real component of the impedance.

Figure 4.5 summarizes the pressure response, Figure 4.6 summarizes the drift and Figure 4.7 summarizes the SNR. To be useful as an EPT the change in response must be large enough for the equipment to register, the drift should be minimized and there should be little noise. Based on these criteria along with the temperature discussion, the

sampling frequency of 500 Hz was selected to carry out additional experiments with the current setup and the real component of the frequency was investigated.

Previous experiments have shown that the ECM response has been linear from the range of 0 to 517 mmHg. A total pressure range experiment was conducted to investigate whether the gel behaves linearly over the entire range or subranges, and also what happens once a threshold is exceeded. Experiments have shown that when a gel is exposed to cyclic pressures up to 517 mmHg, the response is linear whether voltage, current or impedance is measured. In Table 4.1, it was shown that the linear response continues to 1034 mmHg, and at some pressure between 1034 and 1550 mmHg the response starts to behave non-linearly. The total change in impedance from 0 to 1550 mmHg was 18 ohms with an initial impedance of 2035 Ω. At 2070 mmHg the impedance jumps up to 791 kΩ and at 2586 mmHg the impedance continues to 69 MΩ. The glass cell housing the gel and electrodes shattered between 2586 and 3100 mmHg, however impedance data was still recorded. With the pressure returning to 0 mmHg, the impedance stayed high at 54 MΩ. The jump from 2035 Ω to 791 kΩ demonstrated that the conductive gelatin fibers in the aerogel electrode became physically damaged by the higher pressure reducing the amount of charge that could conduct from the aluminum to the bulk solution. As the pressure increased, more damage was reflected in the further increase in impedance up to 69 MΩ. As the pressure was relieved, the impedance dropped down to 54 MΩ at 0 mmHg instead of the initial 2035 Ω indicating that the damage to the gelatin fibers was permanent.

The last test that was performed compared the effects of pressure to an EPT submerged in simulated gastric fluid to an EPT suspended above the fluid. This test was

designed to emulate the placement of the EPTs in two regions of the gastrointestinal tract; the esophagus and the stomach. The EPTs had exposed surfaces of the gelatin to either air or simulated gastric fluid. Figure 4.8 shows the impedance of the EPTs as a function of time after being electrolyzed. The impedance of the EPT submerged in simulated gastric fluid drops by 86% after 24 hours, while the impedance of the EPT suspended in air decreases by 35%. It has already previously been shown that the OCV of a circuit will drop immediately after electrolysis due to the concentration differences on the electrode surface and in the bulk solution without the presence of an applied electric field. However, the impedance of the EPT in the gastric fluid drops much quicker. This is due to ionic migration in the both the hydrogel and the aerogel of the ECC. With more charge conductors from the ionic migration in the ECC the impedance will decrease. Hydrogen ions theoretical have an opposing effect. During the processing of gelatin molecules the hydrogen ions are responsible for attacking and breaking the covalent bonds. Breaking these bonds in the aerogel has been shown in the high pressure test to increase the impedance of the system, therefore if any of the covalent bonds were broken in the ECC, it had a negligible effect that was dominated by the increase in charge conduction. In Figure 4.9 the pressure response in both the air EPT and the gastric EPT started to level off after 4 hours, however, in the gastric EPT the response increased during the first 4 hours suggesting that a larger response can be obtained by raising the concentration of charge carriers in the bulk solution above the native amount. Another notable difference in between the impedance of the EPT in the gastric fluid and the EPT in air is the drift. Figures 4.10 and 4.11 show the pressure response to three square wave pressure inputs. The drift in the EPT is much shallower that that of the air. This

demonstrates that the saturating the ECC with charge carriers will have a more stable response.

4.6 Conclusions

This investigation demonstrated several important parameters necessary to utilize an EPT for GI pressure sensing. The useful range of pressure that the EPT may be useful was determined. The ECM response has been shown to be linear for the range of 0 to 1034 mmHg which exceeds the physiological range of 0 to 300 mmHg in the GI tract. Next, this investigation demonstrated several principals that can be combined to reduce pressurization drift. These items are: (1) using the EPT at least four hours following electrolysis; (2) applying a constant voltage; (3) applying an AC signal relative to the OCV; (4) carefully selecting a frequency that minimizes drift; (5) measuring the real component of the impedance; and (6) increasing the concentration of charge carriers in the ECC. The precise values for each of these items will vary from system to system and will depend on the constraints of the system for which the EPT is designed for.

5 Conclusion

The purpose of this study to was to examine EPTs and their potential use in biomedical applications. Each of these chapters built upon one another filling the void of information in this area. It was determined that the ECM response to pressure is due to the change in surface area of the electrode. Electrolysis in a hydrogel ECC generates an aerogel rather than a single phase gas bubble at the electrodes. The change in surface area of the aerogel/hydrogel interface is linearly related to pressure, and thus the ECM response is also linearly related to applied pressure. The EPT was investigated *in vitro* emulating the physiologic conditions of the GI tract. Several techniques were established to control the sensitivity and accuracy of the response.

A new material system was established raising the voltage response density for ECM systems by 4-orders of magnitude. Additionally, this investigation definitively shows that an ECM response occurs in an ECC only when bubbles are present. This response has been shown through EIS to occur at the electrode interface, and not in the bulk solution. Through derivation of the governing electrochemical equations of the EDL, it was shown that this response is due to a change in the surface area of the electrode.

Investigation of the surface area of an electrolyzed ECC put forth two conclusions. First, the electrolysis in a gelatin hydrogel generates an aerogel rather than single phase gas bubbles. Second, the change in surface area of the aerogel in contact

with the bulk solution is linearly related to the applied pressure. These findings are necessary to support the overall hypothesis that the ECM response to pressure is due to a change in the surface area of the aerogel electrodes. The response was found to be linear for the range of 0 to 280 mmHg, which is in the useful range for medical device applications [52].

This investigation demonstrated several important parameters necessary to utilize an EPT for GI pressure sensing. The useful range of pressure that the EPT may be useful was determined. The ECM response has been shown to be linear for the range of 0 to 1034 mmHg which exceeds the physiological range of 0 to 300 mmHg in the GI tract. Next, this investigation demonstrated several principals that can be combined to reduce pressurization drift. These items are: (1) using the EPT at least four hours following electrolysis; (2) applying a constant voltage; (3) applying an AC signal relative to the OCV; (4) carefully selecting a frequency that minimizes drift; (5) measuring the real component of the impedance; and (6) increasing the concentration of charge carriers in the ECC. The precise values for each of these items will vary from system to system and will depend on the constraints of the system for which the EPT is designed for.

Future studies will be needed to investigate the mechanical properties of gelatin aerogels. In order to be used as an EPT, hysteresis and long term degradation studies are necessary. More studies are also needed in the preparation of the gelatin hydrogels, ionic concentration needs to be investigated as well as preparation of aerogels with air, rather than elemental oxygen and hydrogen.

References

[1] C. S. Smith, "Piezoresistance effect in germanium and silicon," *Physical Review* vol. 94, pp. 42–49, 1954.

[2] D. L. Kendall, "On etching very narrow grooves in silicon," A*pplied Physics Letters* vol. 26, pp. 195–198, 1975.

[3] K. E. Bean, "Anisotropic etching of silicon," *IEEE Transactions on Electron Devices* vol. 25 pp. 1185–1193, 1978.

[4] E. Bassous, "Fabrications of novel three-dimensional microstructures by the anisotropic etching of (100) and (110) silicon," *IEEE Transactions on Electron Devices* vol. 25 pp. 1178–1185, 1978.

[5] W. P. Eaton and J. H. Smith , "Micromachined pressure sensors: Review and recent developments," *Smart Materials and Structures* vol. 6, pp. 530-539, 1997.

[6] D. Wagner, J. Frankenberger and P. Deimel, "Optical pressure sensor using two Mach–Zehnder interferometers for the TE and TM polarizations," *Journal of Micromechanics and Microengineering* vol. 4, pp. 35–39, 1994.

[7] J. A. Dzuiban, A. Gorecka-Drzazga and U. Lipowics, "Silicon optical pressure sensor," *Sensors Actuators A* vol. 32, pp. 628–631, 1992.

[8] Y. Osada, J. P. Gong, and K. Sawahata, "Synthesis, mechanism, and application of an electro-driven chemomechanical system using polymer gels," *Journal of Macromolecular Science* vol. A28, pp. 1189-1205, 1991.

[9] Y. Osada and J. Gong, "Soft and wet materials: Polymer gels," *Journal of Advanced Materials* vol. 10, pp. 827-837, 1998.

[10] W. Takashima, K. Hayasi and K. Kaneto, "Force detection with Donnan equilibrium in polypyrrole film," *Journal of Electrochemical Communications* vol. 9, pp. 2056-2061, 2007.

[11] T. F. Otero, J. J. L. Cascales, and G. V. Arenas, "Mechanical characterization of free-standing polypyrrole film," *Materials Sieince and Engineering C-Biometric and Supramolecular Systems* vol. 27, pp. 18-22, 2007.

[12] "Standard Methods for the Sampling and Testing of Gelatins," *Gelatin Manufacturers Institute of America, Inc.*, 501 fifth Ave., Room 1015, New York, NY.

[13] J. E. Strassner and P. Delahay, "Polarographic study of the effect of gelatin on the kinetics of irreversible electrode process," *Journal of the American Chemical Society* vol. 74, pp. 6232-6235, 1952.

[14] D. F. Vieira, C. O. Avellaneda and A. Pawlicka, "Conductivity study of a gelatin-based polymer electrolyte," *Electrochimaica Acta* vol. 53, pp. 1404-1408, 2007.

[15] S. W. John, G. Alici, and G. M. Spinks, "Towards fully optimized conducting polymer bending sensors: the effect of geometry," *Smart Materials and Structures* vol. 18 2009.

[16] H. B. Bohidar, and S. S. Jena, "Kinetics of sol-gel transition in thermoreversible gelation of gelatin," *Journal of Chemical Physics* vol. 98, pp. 8970-8977, 1993.

[17] A. J. Bard, "Encyclopedia of Electrochemistry of the Elements," M. Dekker, New York, pp. 71, 1973.

[18] W. Z. Nernst, *Physical Chemistry* vol. 4, pp. 129, 1869.

[19] F. Scholz, "Electroanalytical Methods," Springer, Verlag Berlin Heidelberg New York, pp. 5, 2002.
[20] E. Barsoukov and J. R. MacDonald, "Impedance Spectroscopy," Wiley, Hoboken, New Jersey, pp. 98, 2005.
[21] J. Randles, "Kinetics of rapid electrode reactions," *Discussions of the Faraday Society* vol. 1, pp. 11-19, 1947.
[22] J. R. MacDonald, "Discrimination between equations of state," *Journal of Research of the National Bureau of Standard Section A-Physics and Chemistry* vol. 5, pp. 441 1971.
[23] M. Sabouri, T. Shahrabi, H. R. Farid, and M. G. Hosseini, "Polypyrrole and polypyrrole-tungstate electropolymerization coatings on carbon steel and evaluating their corrosion protection performance via electrochemical impedance spectroscopy," *Progress in Organic Coatings* vol. 64, pp. 429-434 2009.
[24] A. Aghaei, M. R. M. Hosseini, M. Najafi, " A novel capacitive biosensor for cholesterol assay that uses an electropolymerized molecularly imprinted polymer," *Electrochimica Acta* vol. 55, pp. 1503-1508, 2010.
[25] C. Deslouis, T. El Moustafid, M. M. Musiani, " Mixed ionic-electronic conduction of a conducting polymer film. Ac impedance study of polypyrrole," *Electrochimica Acta* vol. 41, pp. 1343-1349, 1996.
[26] J. E. Strassner and P. Delahay, "Polarographic study of the effect of gelatin on the kinetics of irreversible electrode process," *Journal of the American Chemical Society* vol. 74, pp. 6232-6235, 1952.
[27] E. Barsoukov and J. R. MacDonald, "Impedance Spectroscopy," Wiley, Hoboken, New Jersey, pp. 6, 2005.
[28] R. b. Darst, "Introduction to Linear Programming," Marcel Dekker, Inc., New York, pp. 6, 1991.
[29] S. Iwamoto, H. Kumagai, "Analysis of the dielectric relaxation of a gelatin solution," *Bioscience Biotechnology and Biochemistry* vol. 62, pp. 1381-1387, 1998.
[30] G. J. Sloggett, N. G. Barton, S. J. Spencer, "Fringing fields in disk capacitors," *Journal of Physics A - Mathematical and General* vol. 19, pp. 2725-2736, 1986.
[31] H. Von Helmholtz, Annuls *of Physics* vol. 89, pp. 221, 1853.
[32] P. Debye, E. Huckel, "The theory of electrolytes." *Phys. Z.* vol. 47, pp. 206, 305, 1923.
[33] E. Klaseboer, C. K. Turangan, and B. C. Khoo, "Dynamic behavior of a bubble near an elastic infinite interface," *International Journal of Multiphase Flow* vol. 32, pp. 1110-1112, 2006.
[34] G. Terrones and P. A. Gauglitz, "Deformation of a spherical bubble in soft solid media under external pressure," *Quarterly Journal of Mechanics and Applied Mathematics* vol. 56, pp. 513-525, 2003.
[35] H. Wang, J. Ma, and W. Zhang, "Effect of film viscoelasticity on the finite deformation of a spherical bubble," *Journal of Applied Physics* vol. 102, pp. Article 074919-1, 2007.

[36] S. Goldman, "Generalizations of the Young-Laplace equation for the pressure of a mechanically stable gas bubble in a soft elastic material," *Journal of Chemical Physics* vol. 131, pp. Article 184502, 2009.
[37] E. A. Guggenheim, "Thermodynamics. An Advanced Treatment for Chemists and Physicists," North-Holland, Amsterdam, Chapter 1, 1967.
[38] S. Kistler, "Coherent expanded aerogels and jellies," *Nature* vol. 127, pp. 741, 1931.
[39] L. Baia, M. Baia, V. Danciu, " Type I collagen-TiO2 aerogel based biocomposites," *Journal of Optoelectronics and Advanced Materials* vol. 10, pp. 933-936, 2008.
[40] A.C. Pierce and G.M. Pajonk, "Chemistry of aerogels and their applications," *Chemical Reviews* vol. 102, pp. 4243-4265, 2002.
[41] M. Giorgetti, S. Passerini, W. H. Smyrl, and M. Berettoni, "Identification of an unconventional zinc coordination site in anhydrous ZnxV2O5 aerogels from X-ray absorption spectroscopy," *Chemistry of Materials* vol. 11, pp. 2257, 1999.
[42] S. Passerini, F. Coustier, M. Giorgetti, and W. H. Smyrl, " Li-Mn-O aerogels," *Electrochemical and Solid State Letters* vol. 2, pp. 483, 1999.
[43] W. Dong, and B. Dunn, " Sol-gel synthesis and characterization of molybdenum oxide gels," *Journal of Non-crystalline Solids* vol. 225, pp. 135, 1998.
[44] S. T. Mayer, R.W. Pekala, and J.L. Kaschmitter, "The aerocapacitor - an electrochemical double-layer energy-storage device," *Journal of the Electrochemistry Society* vol. 140, pp. 446, 1993.
[45] R. W. Pekala, J. C. Farmer, C. T. Alviso, T. D. Tran, S. T. Mayer, J. M. Miller, and B. Dunn, "Carbon aerogels for electrochemical applications," *Journal of Non-crystalline Solids* vol. 225, pp. 74, 1998.
[46] R. Saliger, U. Fischer, C. Herta, and J. Fricke, " High surface area carbon aerogels for supercapacitors," *Journal of Non-crystalline Solids* vol. 225, pp. 81, 1998.
[47] R. W. Pekala, and C. T. Alviso, "Carbon aerogels and xerogels," *Novel Forms of Carbon* vol. 270, pp. 3, 1992.
[48] R. W. Pekala, L. W. Hrubesh, T. M. Tillotson, C. T. Alviso, J. F. Poco, and J. D. LeMay, " A comparison of mechanical-properties and scaling law relationships for silica aerogels and their organic counterparts," *Mechanical properties of porous and cellular materials* vol. 207, pp. 197, 1991.
[49] T. Woignier, and J. Phalippou, *Applied Physics Review* vol. 24, pp. 179, 1989.
[50] G. W. Scherer, D. M. Smith, X. M. Qui, J. M. Anderson, "Compression of aerogels," *Journal of Non-crystalline Solids* vol. 186, pp. 316-320, 1995.
[51] Y. Lentz, L. Worden, T. Anchordoquy, and C. S. Lengsfeld, "DNA acts as a nucleation site for transient cavitation in the ultrasonic nebulizer," *Journal of Pharmaceutical Science* vol. 95, pp. 607-619, 2006.
[52] C. Stendal, "Practical Guide to Gastrointestinal Function Testing," Blackwell Science Ltd., Malden, 1997.
[53] B. Lindgren, and L. Janzon, "Prevalence of swallowing complaints and clinical findings among 50-79-year-- old men and women in an urban population," Dysphagia vol. 6, pp. 187-192, 1991.

[54] L. Tibbling, and B. Gustafsson, "Dysphagia and its consequences in the elderly," *Dysphagia* vol. 6, pp. 200-202, 1991.
[55] M. F. Brin, and D. Younger, "Neurologic disorders and aspiration," *Otolaryngol Clin North Am* vol. 21 pp. 691-699, 1988.
[56] M. R. Spieker, "Evaluating dysphagia," *American Family Physician* vol. 61 pp. 3639, 2000.
[57] J. E. Pandolfino, M. A. Kwiatek, T. Nealis, W. Bulsiewicz, J. Post J,and P. J. Kahrilas , "Achalasia: A new clinically relevant classification by high-resolution manometry," *Gastroenterology* vol. 135 pp. 1526-1535, 2008.
[58] F. M. S. McConnel, D. Hood, K. Jackson, and A. O'Conner, "Analysis of intrabolus forces in patients with Zenkers diverticulum," *Laryngoscope* vol. 104 pp. 571-581, 1994.
[59] J. Brun, L. Bengtsson, and H. Sorngard, "Diagnostic test and treatment of acid related GERD in a general practice population," *GUT* vol. 41 pp. A63-A64, 1997.
[60] A. Aubert, A. Ferre A, F. Bloch, J. N. Fiessinger, M. Vayssairat, and J. P. Pettite, "Which manometric criteria are useful in defining scleroderma esophagus," *Gastroenterologie Clinique et Biologique* vol. 13 pp. A66, 1989.
[61] J. A. Almario, E. Gorospe, P. Rajan, C. Winter, A. Kage, T. Wittenberg , C. Munzenmayer, G. Hager, and M. Canto "Accuracy and interobserver agreement among experts and non-experts for the diagnosis of barrett's esophagus (BE) and related neoplasia (BERN) using high resolution white light endoscopy with limited magnification," *American Journal of Gastroenterology* vol. 104 pp. S532, 2009.